MISR Global Aerosol Product Assessment by Comparison with AERONET

Ralph A. Kahn[1], Barbara J. Gaitley[2], Michael J. Garay[3], David J. Diner[2], Thomas F. Eck[4], Alexander Smirnov[5], and Brent N. Holben[1]

[1]Laboratory for Atmospheres, NASA Goddard Space Flight Center
Greenbelt, MD 20771

[2]Jet Propulsion Laboratory, California Institute of Technology
4800 Oak Grove Drive, Pasadena CA 91109

[3]Raytheon Company
299 N. Euclid Ave., Suite 500
Pasadena, CA 91101

[4]Goddard Earth Sciences and Technology Center,
University of Maryland Baltimore County, Baltimore MD

[5]Sigma Space Corporation, Lanham, MD

Submitted: The Journal of Geophysical Research, Atmospheres

June 2010

Abstract

A statistical approach is used to assess the quality of the MISR Version 22 (V22) aerosol products. Aerosol Optical Depth (AOD) retrieval results are improved relative to the early post-launch values reported by *Kahn et al.* [2005a], varying with particle type category. Overall, about 70% to 75% of MISR AOD retrievals fall within 0.05 or 20% × AOD of the paired validation data, and about 50% to 55% are within 0.03 or 10% × AOD, except at sites where dust, or mixed dust and smoke, are commonly found. Retrieved particle microphysical properties amount to categorical values, such as three groupings in size: "small," "medium," and "large." For particle size, ground-based AERONET sun photometer Angstrom Exponents are used to assess statistically the corresponding MISR values, which are interpreted in terms of retrieved size categories. Coincident Single-Scattering Albedo (SSA) and fraction AOD spherical data are too limited for statistical validation. V22 distinguishes two or three size bins, depending on aerosol type, and about two bins in SSA (absorbing vs. non-absorbing), as well as spherical vs. non-spherical particles, under good retrieval conditions. Particle type sensitivity varies considerably with conditions, and is diminished for mid-visible AOD below about 0.15 or 0.2. Based on these results, specific algorithm upgrades are proposed, and are being investigated by the MISR team for possible implementation in future versions of the product.

1. Introduction

Since the launch of the NASA Earth Observing System (EOS) satellites, enormous strides have been made in Aerosol Optical Depth (AOD) remote sensing over land and water [e.g., *Martonchik et al.*, 2009; *Kahn et al.*, 2005a; *Remer et al.,* 2005; 2008]. The global data sets produced by the Multi-angle Imaging SpectroRadiometer (MISR) and MODerate resolution Imaging Spectroradiometer (MODIS) instruments have contributed to reducing uncertainties in aerosol transport and radiative impact modeling [e.g., *Zhang and* Christopher, 2003; *Kinne et al.,* 2006; *Yu et al.*, 2006; *Kim and Ramanathan,* 2008; *Chen et al.,* 2009], leading, for example, to a reduction in the overall climate forcing uncertainty attributed to aerosols [*IPCC*, 2007; *Haywood and Schulz*, 2007].

However, significant further reduction in aerosol climate impact assessment depends upon retrieving aerosol type along with AOD. MISR-retrieved aerosol type has been used in a range

of applications, including particle shape [*Kalashnikova and Kahn*, 2006; *Liu et al.,* 2007a; b], and combinations of size distribution and single-scattering albedo (SSA) constraints [*Chen et al.*, 2008], size and shape [*Kalashnikova and Kahn,* 2008; *Dey and Di Girolamo, 2010*; *Pierce et al.,* 2010], and all three microphysical property constraints [*Kahn et al., 2008*]. In addition to the intrinsic value of such information for helping determine particle composition and origin, and for mapping aerosol transport, deposition, and evolution, particle type is among the key factors determining AOD retrieval accuracy itself [e.g., *Kahn, et al., 2007a*].

MISR was launched into a sun-synchronous polar orbit in December 1999, aboard the NASA EOS Terra satellite. Terra crosses the equator on the descending node at about 10:30 AM local time. MISR is unique among the EOS-era satellite instruments in having a combination of high spatial resolution, a wide range of along-track view angles, and high-accuracy radiometric calibration and stability [*Diner et al.*, 1998]. Global coverage (to ±82° latitude) is obtained about once per week.

MISR measures upwelling short-wave radiance from Earth in four spectral bands centered at 446, 558, 672, and 866 nm, at each of nine view angles spread out in the forward and aft directions along the flight path, at 70.5°, 60.0°, 45.6°, 26.1°, and nadir. Over a period of seven minutes, as the spacecraft flies overhead, a 380-km-wide swath of Earth is successively viewed by each of MISR's nine cameras. As a result, the instrument samples a very large range of scattering angles – between about 60° and 160° at mid latitudes, providing information about aerosol microphysical properties. These views also capture air-mass factors ranging from one to three, offering sensitivity to optically thin aerosol layers, and allowing aerosol retrieval algorithms to distinguish surface from atmospheric contributions to the top-of-atmosphere (TOA) radiance.

The MISR Standard aerosol retrieval algorithm runs in an operational, fully automatic mode. It reports AOD and aerosol type at 17.6 km resolution, by analyzing data from 16 x 16 pixel regions of 1.1 km-resolution, MISR top-of-atmosphere radiances [*Diner et al.*, 2006; *Kahn et al.,* 2009; *Martonchik et al.,* 2009]. Pre-launch studies predicted that MISR sensitivity to AOD and particle properties would vary with conditions. At least over dark water, for good retrieval conditions and AOD at mid-visible wavelengths larger than about 0.15, MISR was expected to distinguish about three-to-five groupings based on particle size, two-to-four groupings in single-scattering albedo (SSA), and spherical vs. non-spherical particles [*Kahn et al.,* 1997; 1998;

2001]. In these studies, we usually modeled good retrieval conditions over water as a uniform, cloud-free scene, with a dark surface having near-surface wind speed around 2.5 m/s; we also tested a range of conditions to assess the robustness of the results.

Using a combination of MISR Standard [*Martonchik et al.,* 1998; 2002; 2009] and Research [*Kahn et al.*, 2001] aerosol retrieval algorithms, several post-launch studies focused on MISR sensitivity to particle properties as well as AOD, for individual cases when specific aerosol types dominate. These studies, covering desert dust [*Kalashnikova et al.,* 2005; *Kalashnikova and Kahn*, 2006; *Kahn et al.,* 2008], biomass burning [*Chen et al.,* 2008], and cirrus [*Pierce et al.,* 2010] cases, generally confirm pre-launch expectations about size, shape, and SSA sensitivity, and add considerable detail to earlier predictions.

Post-launch statistical assessments of the MISR aerosol products have so far concentrated on AOD [e.g., *Abdou et al.*, 2005; *Christopher and Wang*, 2004; *Diner et al.,* 2001; *Jiang et al.*, 2007; *Kahn et al.* 2005a; *Liu et al.,* 2004; *Martonchik et al.*, 2004]. For example, *Kahn et al.* [2005a; henceforth Paper 1] evaluated the Version 12 early post-launch aerosol product by comparing MISR AOD with a two-year, globally distributed set of AErosol RObotic NETwork (AERONET) surface-based sun photometer measurements [*Holben et al.,* 1998]. Paper 1 concluded that for Version 12 of the MISR algorithm, about two-thirds of the MISR-retrieved AOD values for which there are coincident AERONET retrievals fall within the larger of 0.05 or 20% × AOD relative to AERONET, and more than a third were within 0.03 or 10% × AOD. The results also suggested that adding to the algorithm climatology more absorbing spherical particles, more realistic dust optical analogs, and a richer selection of multi-modal aerosol mixtures would reduce the remaining AOD discrepancies with AERONET for MISR retrievals over land; in addition, refining instrument low-light-level calibration would reduce or eliminate a small but systematic offset in Maritime AOD values.

Version 22 (V22) incorporates many of the suggested upgrades, including a more realistic medium-mode desert dust optical model [*Kalashnikova et al.*, 2005; see also Table 2], small-medium, spherical particles having mid-visible SSA of 0.8 and 0.9, and more multi-modal aerosol distributions in the standard algorithm climatology, along with other algorithm adjustments described in the MISR product documentation [see *http://eosweb.larc.nasa.gov/PRODOCS/misr/table_misr.html*]. In addition, the MISR band-to-band and camera-to-camera radiometric calibration has been improved, which partly corrected

the low-AOD bias relative to AERONET [*Bruegge et al., 2007*; *Diner et al., 2004*; *Kahn et al.,* 2005b]. As before, the V22 algorithm reports the best estimate spectral AOD as "regional mean" values, which are averages, with equal weight, of the AOD obtained for each mixture in the algorithm climatology that pass the acceptance criteria. But the best estimate particle size, SSA, and fraction AOD spherical are obtained from the aerosol mixture having TOA radiances with the lowest residuals relative to the MISR observations. The AOD associated with the lowest-residual mixture is also reported in the data product. The full MISR data record from February 2000 to the present has been reprocessed to V22.

In this paper we assess the quality of the MISR V22 Level 2AS Aerosol product over land and water, and make suggestions for additional algorithm refinements. Further assessment and product refinement are justified by the exacting demands on AOD particle type accuracy for air quality and material transport studies, and for evaluating direct aerosol radiative forcing regionally and globally. The ten-year record is also beginning to make time-series and trend analyses worth pursuing with MISR data. Fortunately, over this period, we have acquired much more validation data, which provide better statistics, cover a wider range of conditions, and include more detailed ground-truth measurements than were available early in the MISR mission. In addition, we have learned a great deal from work already done with the MISR products, by the instrument team and many others.

Our approach is to compare the MISR data with coincident observations from 81 globally distributed AERONET sites over eight years. As in Paper 1, we take a statistical approach, and stratify the observations by season and expected aerosol type. But here, in addition to comparing the new MISR-retrieved mid-visible AOD, we study Angstrom Exponent (ANG) in light of AERONET direct sun spectral AOD measurements, and explore the implications for retrieved particle components and mixtures. These are all total-column effective values, as there is no height-resolved information in either the MISR or the AERONET aerosol retrievals (though the MISR stereo product includes aerosol plume heights in wildfire, volcanic, and desert dust near-source regions [*Kahn et al.,* 2007b]). Note also that, as with Paper 1, this is not a test of MISR cloud masking, because coincidences must pass both the MISR and AERONET cloud masks to be included in this study. MISR cloud mask performance is the subject of separate studies [e.g., *Zhao et al.*, 2009].

166 This paper is organized as follows: Section 2 describes how the MISR and AERONET data were
167 selected and processed, and gives an overview of sampling statistics. Section 3 summarizes
168 AOD performance; trends and patterns in the AOD differences are identified, stratified by
169 location and season so as to separate typical aerosol types, and are compared with results from
170 the early post-launch product studied in Paper 1. Section 4 looks in detail at the particle
171 properties reported in the MISR aerosol product, investigates outliers, and explores possible
172 causes for the observed behavior. Section 5 provides a summary of results and recommendations
173 for further product refinements, and the final section presents conclusions.
174
175

176 2. Data Selection and Analysis Approach

177
178 We compare MISR-retrieved aerosol quantities with coincident AERONET direct-sun and sky-
179 scan results. The data involved are described in this section.
180

181 2.1. AERONET Surface-based Sun Photometer Network Data

182
183 AERONET direct-sun measurements are taken automatically with ground-based CIMEL sun
184 photometers every 15 minutes during daylight hours. Standard processing includes operational
185 cloud screening [*Smirnov et al.*, 2000] and generates AOD from the direct transmission.
186 AERONET sun photometers are inter-calibrated with reference CIMELs, which in turn are
187 calibrated using the Langley method at Mauna Loa Observatory, Hawaii, in bands nominally
188 centered at about 340, 380, 440, 500, 675, 870, and 1020 nm, plus a column water vapor channel
189 [*Holben et al.*, 1998; *http://aeronet.gsfc.nasa.gov/*]. For this study, we work with Version 2
190 AERONET data, at Level 2.0 (Level 1.5 AERONET AOD data are cloud-screened values, but
191 are calibrated based on a single pre-deployment comparison with a standard reference, and can
192 have an uncertainty of 0.02 or greater. The Level 2 data, for which a second, post-deployment
193 comparison is also used in calibration along with manual validation checks, are somewhat less
194 frequent overall, but they have AOD measurement accuracy of ~0.01 in the mid-visible [*Eck et*
195 *al.,* 1999].) Unlike Paper 1, we include here cases for which mid-visible AOD values exceed
196 1.0, in part to take advantage of increased AERONET particle property retrieval accuracy.
197 However, such cases are relatively rare in the coincident data set, and often involve dust or
198 smoke plumes having considerable spatial variability; this exacerbates sampling differences and

reduces the utility of the comparison for MISR retrieval validation (see Paper 1). We also include comparisons between MISR AOD and coincident measurements from AERONET's ship-based Marine Aerosol Network (MAN) sun photometers [*Smirnov et al.*, 2009]. These observations are obtained with hand-held Microtops instruments; the data are processed similarly to the CIMEL direct sun measurements, but have slightly reduced measurement accuracy of ~0.02. MAN provides additional dark ocean AOD and ANG cases, which are especially valuable here because there are very few MISR-AERONET coincidences in these situations.

ANG is derived from the spectral AOD values. It is defined as the negative slope of the least-squares linear fit of ln (AOD) vs. ln (wavelength). ANG is a single variable related to the particle size distribution, though its interpretation is complicated, in part when non-linearity in spectral AOD dependence is significant, and especially when multi-modal aerosol distributions are present [e.g., *Schuster et al.,* 2006]. AERONET AOD and ANG are both derived solely from direct-sun extinction measurements; as such, the primary uncertainty in these values when compared to MISR observations arises from sampling differences, though these can be considerable, especially near aerosol sources, where particle concentrations can vary greatly. Other uncertainties include differences in the wavelengths measured by each instrument, and for ANG, the fact that it is derived from the slope of multiple observations, each having its own measurement errors.

To facilitate comparisons, note that unlike the linear interpolation applied for Paper 1, all AERONET AOD values used in this paper were interpolated to the MISR band effective wavelengths using a second-order polynomial fit to ln (AOD) vs. ln (wavelength), as recommended by *Eck et al.* [1999]. As before, the AERONET Angstrom Exponents are calculated from the spectrally interpolated and temporally averaged direct-sun AERONET AOD values at the four MISR wavelengths, using the same least-squared fitting approach adopted for the MISR data themselves.

The AERONET instruments also perform sky scans in the principal plane and across the almucantar at 440, 675, 870, and 1020 nm about once per hour, from which aerosol size distributions and refractive indices are derived [*Dubovik and King*, 2000; *Dubovik et al.*, 2006]. Retrieved size is reported as a relative, volume-weighted quantity in 22 bins of particle radius, spread logarithmically between 0.05 and 15 microns. Size distributions are also provided in the AERONET standard product as one medium-mode and one coarse-mode log-normal parameter,

fit to the 22-bin histogram [*Dubovik and King*, 2000]. A combination of direct sun and sky-scan data is used to retrieve spectral indices of refraction and SSA, though they are considered of high quality only when the solar zenith angle is greater than 50° and the AOD at 440 nm is 0.4 or above [*Dubovik et al.*, 2000].

Figure 1 shows the locations of the 81 AERONET sites used in this study. These sites were selected for their geographic diversity, and for providing generally good-quality and well-populated data records during the analysis period (Table 1). The sites are classified as Dusty, Biomass Burning, Continental, Urban, Maritime, or Hybrid (smoke + dust), based on the expected dominant aerosol type, at least during some seasons. (Independent, event-by-event classification of aerosol type is possible only on rare occasions, primarily when *in situ* measurements from field campaigns are available, or when major smoke or dust plumes fall within the coincident MISR-AERONET sampling region.) Although component particle microphysical properties vary within each category, these six groupings represent broad classes of aerosol air mass types we expect to distinguish globally with MISR [*Kahn et al.,* 2001], and to some extent, they represent different passive remote-sensing retrieval challenges.

2.2. MISR Data Attributes, and Co-location with Surface Stations

The MISR Standard aerosol retrieval algorithm searches a database of TOA radiances simulated for the MISR channels, solar position, and viewing geometries, assuming a range of candidate aerosol mixtures and optical depths, and compares them with the observed radiance imagery [*Martonchik et al.*, 1998; 2009]. Component particle optical properties assumed in the algorithm cover ranges of "small," "medium," and "large," non-absorbing and absorbing, spherical and randomly oriented non-spherical types (Table 2). A limited selection of mixtures of these components is used in the V22 algorithm, as given in Table 3. The entries are organized so that, for most of this table, each decade contains mixtures among a fixed set of components, in systematically varying proportions. Exclusively spherical, non-absorbing components are found in Mixtures 1 to 30, with the fine-mode components having progressively larger sizes for Mixtures 1-10, 11-20, and 21-30. Mixtures 31-40 and 41-50 include spherical, absorbing fine-mode components, with mid-visible SSA=0.90 and 0.80, respectively, and 51-74 are mixtures that contain non-spherical medium and coarse-mode dust optical analogs. Overall sensitivity to particle type AOD fraction is around 0.2 for AOD $\gtrsim$ 0.15, and diminishes when AOD is lower [*Chen et al.,* 2008; *Kalashnikova and Kahn*, 2006].

Aerosol retrieval success is measured by the degree to which observed multi-angle, multi-spectral TOA radiances match modeled radiances, using several chi-squared criteria [e.g., *Kahn et al.,* 1998; *Martonchik et al.,* 1998; 2009]. In V22, the MISR ANG is obtained from the mean optical depths of all successful mixtures, calculated separately at each MISR wavelength. As with the AERONET data, the MISR aerosol retrievals used here meet the cloud-free and other high-data-quality standards set by the experiment team [e.g., *Diner et al.,* 2006; *Kahn et al.*, 2009; summarized in the MISR Data Quality Statement distributed on-line with MISR data products; *http://eosweb.larc.nasa.gov/PRODOCS/misr/table_misr.html*]. MISR Level 2 aerosol retrievals use only data that pass angle-to-angle smoothness and spatial correlation tests [*Martonchik et al.*, 2002], as well as stereoscopically derived cloud masks and adaptive cloud-screening brightness thresholds [*Di Girolamo and Wilson*, 2003; *Zhao and DiGirolamo,* 2004].

As in Paper 1, we searched the V22 product for overflights having successful retrievals either in the MISR 17.6 km retrieval region containing each AERONET station selected (the "central" region), or in one or more of the eight retrieval regions surrounding the central one. We use both the central and all available surrounding region retrievals for comparison with AERONET AOD; values obtained for the surrounding regions help assess AOD spatial variability on 20-to-50 km scales. We also required in Paper 1 that the AERONET time series for each coincidence include at least one AOD measurement during the hour before the MISR overpass, and at least one during the hour after the overpass. We do the same here.

A fundamental difference between the MISR and AERONET AOD observations is that MISR acquires instantaneous data over an entire 20-to-50 km study area (one central + eight surrounding 17.6 km retrieval regions), whereas AERONET obtains a time-series of point data at each surface station. For each event, we averaged with equal weight all available AERONET AOD retrievals for a two-hour window centered on the MISR overpass time. This crudely covers the period during which aerosols advecting at 5-to-15 m/s would traverse the MISR study area, though not necessarily sampling it uniformly. We rely on the large number of events included in this study to average out any subtle sampling anomalies, and we highlight as outliers any individual pathological cases. We also take the likely limitations of these assumptions into consideration when drawing conclusions.

There are far fewer once-hourly AERONET sky-scan particle property retrievals than AOD values. To effect comparisons with MISR, we accepted any case where at least two good-quality sky-scan results fall within a four-hour window centered on MISR overpass time. If there are multiple, successful AERONET sky-scan retrievals within the window, SSA values are averaged. An assumption underlying this approach is that within an aerosol air mass, particle type varies less than AOD; there is some observational support for this assumption [e.g., *Anderson et al.,* 2003], though there are likely to be exceptions [e.g., *Kahn et al., 2007a*], especially near sources, or when multiple aerosol layers of different types are present. In practice, about 80% of the cases included have at least one measurement on each side of overpass time; the rest have at least two measurements on one side of the overpass window.

Table 4 summarizes the sampling statistics for the entire data set, stratified by season and expected aerosol type. Over eight years, we obtained 5,156 coincident, central MISR-AERONET AOD observations that met the data selection criteria, and 2,130 central sky-scan results. There are over 1,300 central AOD events for each of Continental and Urban aerosol sites, over 650 each for Biomass Burning and Dusty, over 600 for Hybrid, and not quite 400 for the Maritime categories. There are about 650 Sky-scan coincidences for Urban, just under 500 for Continental, about 300 each for Biomass Burning, Dusty, and Hybrid, and 81 for Maritime. Frequent cloud contamination and relatively few available sites contribute to lower sampling for Maritime sites.

Also shown in Table 4 are the numbers of events in each category for which the lowest residual aerosol mixture in the MISR V22 product contained (a) only spherical, non-absorbing particles, (b) both spherical absorbing and non-absorbing particles, or (c) both non-spherical mineral dust and spherical non-absorbing particles. Although the lowest residual mixture is generally unique, more than one mixture can meet the chi-squared criteria for a successful retrieval. These data are discussed in the next section.

3. MISR AOD Retrieval Assessment

Figure 2 and Table 5 report the overall group average MISR-AERONET mid-visible (558 nm) AOD difference statistics by probable aerosol category, as well as summary statistics derived in

Paper 1 based on similar aerosol-type groupings for the Version 12 algorithm. Table 5 also contains the corresponding site-specific data. The figure compares the AERONET values with the MISR central and surrounding retrieval regions for each category. Of 5,156 coincidences, 125 significant outliers (2.4%), where the MISR AOD is more than 2.5 times higher than AERONET, and 68 (1.3%) where the MISR AOD is less than 60% of the corresponding AERONET value, have been removed from the statistics of Table 5 and Figure 2. Of the high outliers, 61% are attributable to spatial and/or temporal scene variability, convolved with the differences between MISR and AERONET sampling, rather than retrieval error. This conclusion is based on variability in the retrieval results from the central vs. surrounding regions, and/or the AERONET time series. About an additional 35% of the high outliers are likely due to variability as well, including cases having nearby scattered or broken cloud. The corresponding values for the low AOD outliers are 63% and 22%, respectively. Sampling outliers can occur if an aerosol plume is found in the MISR image but misses the AERONET field-of-view (FOV), or if a plume fills the AERONET FOV but accounts for only a small fraction of the MISR retrieval region. So for both the high and low outliers of significant magnitude, over 80% are likely due to sampling differences. A similar result was obtained in Paper 1. About 15% of the 68 MISR low outliers in this data set are cases where MISR adopted an unduly high particle SSA compared to AERONET. Other factors, including algorithmic issues, account for the remaining cases; these issues are explored in more detail below.

In Figure 2, focus first on the position along the horizontal axis of the filled diamond and circle symbols, connected with solid lines. These represent the category-specific percent of cases for which the MISR central AOD is within 0.05 or 20% × AOD, and 0.03 or 10% × AOD, of the near-coincident AERONET value, respectively. The results vary considerably, depending on category. *For V22, about 70% to 75% fall within 0.05 or 20% × AOD of the validation data, and about 50% to 55% meet the 0.03 or 10% × AOD criterion, except in the Dusty and Hybrid (smoke + dust) categories.* The open diamond and circle symbols and dashed lines plot the corresponding values for the V12 algorithm. For the 0.05 or 20% × AOD criterion, the V22 values are about 10%, 7%, and 6% higher than those for V12 for the Biomass Burning, Continental, and Maritime aerosol categories, respectively, reflecting improvements made to the retrieval algorithm as mentioned in Section 1. For the Dusty category, the agreement is about 5% poorer, due in part to a lack of medium-mode spherical particles in the V22 component set (Section 4.2 below); the other categories were not independently tracked in the earlier, smaller

366 data set. Similar relationships among the categories, and between the V12 and V22 results, are
367 found for the more stringent 0.03 or 10% × AOD criterion.
368
369 Placement along the vertical axis in Figure 2 compares the AERONET two-hour-averaged values
370 with the spatial average of MISR AOD results for the central and as many of the eight
371 surrounding regions as have successful retrievals, and with those for the central region alone.
372 The difference plotted accounts to some degree for variability; for points above the zero line, the
373 larger-spatial-scale (~50 km) central + surrounding region average produces systematically better
374 agreement with AERONET than the single-region (17.6 km) central comparison. For points
375 below the zero line, there is an advantage for the MISR retrieval regions to be collocated with the
376 AERONET site as closely as possible. These results by category are statistically fairly robust, as
377 each large symbol represents hundreds to over 1,000 MISR-AERONET comparisons, though the
378 sampling varies significantly for individual sites (Table 5).
379
380 Focusing again on the filled symbols, the larger-scale averaging produces 2 to 3% better
381 agreement for the Continental and Biomass Burning categories, 5% better agreement for Dusty,
382 and almost 8% for Maritime, whereas the central region provides better agreement for the Urban
383 class and marginally better agreement for the less-well-sampled Hybrid class. In Urban regions,
384 where AOD variability is expected to be dominant on short spatial scales, the central regions
385 have a systematic advantage in representing the AERONET two-hour-window measurements
386 [*Jiang et al.*, 2007]. Site-specific values illustrate this point. For example, Mexico City is
387 responsible for an Urban outlier that would plot along the vertical axis in Figure 2 at about -32%
388 (Table 5). By contrast, for Maritime situations, where aerosols are generally more uniform on 10
389 km to 100 km scales, the larger spatial averaging reduces the impact of serendipitous aerosol air
390 mass edges and AOD gradients sampled differently by the satellite and surface stations [*Kahn et*
391 *al.*, 2007a, Section 3.2]. Similarly, at Continental sites such as El Arenosillo in southern Spain
392 and Arica in northern Chile, regional averaging produces significantly better agreement with the
393 AERONET time series. Site-to-site differences in regional source characteristics, topography,
394 and meteorology account for the scatter among AERONET stations within each category, but
395 overall, the variability patterns are distinct, and consistent with expectations.
396
397 Figure 3 looks in more detail at the MISR-AERONET mid-visible AOD comparisons, showing
398 both scatter and difference plots, stratified by season and by the six expected aerosol air mass
399 type groupings described above. The middle row of this figure focuses on the low-AOD range of

400 the scatter plots from the top row, and uses open circles to improve the visibility of individual
401 events.
402
403 The data exhibit many expected patterns, such as Maritime AOD generally below 0.3, and high
404 AOD events, in excess of 0.6, occurring preferentially for the Biomass Burning, Dusty, Urban,
405 and Hybrid categories. The quantitative ranges of values are somewhat higher than
406 corresponding ones in Paper 1, due to much greater sampling in the current data collection,
407 which captures a broader spectrum of naturally occurring conditions. Although these MISR
408 validation data subsets were chosen for coincidence with AERONET rather than being optimized
409 to represent the "global-average" AOD, they cover a diversity of situations. As such, they
410 illustrate one reason for obtaining longer-term, climate-quality data records; as larger data sets
411 are acquired, it will become possible to separate with greater confidence sampling effects from
412 natural patterns, trends, and extreme events, and an increasingly robust environmental picture
413 will emerge. This is true for the validation process itself as well. Having provided an overview
414 based on Figures 2 and 3, we now explore individual strata in more detail.
415
416 **3.1. AOD Performance at Very Low AOD and Maritime Sites**
417
418 When AOD is very low, MISR tends to overestimate AOD, for a small but significant fraction of
419 cases in all aerosol types. The concentrations of points above the zero lines in the difference
420 plots along the bottom row of Figure 3, when AOD is low, illustrate this condition. The middle
421 row of plots in Figure 3 reveals a gap of about +0.025 in the MISR mid-visible AOD values near
422 zero AOD. This gap does not appear in the AERONET validation data, as is especially clear for
423 the well-sampled Biomass Burning and Continental category plots. Comparison between MISR
424 and a much larger number of coincident MODIS/Terra observations shows similar MISR
425 behavior [Figure 5 of *Kahn et al.,* 2009].
426
427 Previous work removed about half of a ~0.05 high bias, evident in the early post-launch (Version
428 12) MISR AOD over-ocean product, when the MISR band-to-band and camera-to-camera
429 calibrations were corrected [*Bruegge et al.*, 2007; *Diner et al.,* 2004; *Kahn et al.,* 2005b]. These
430 corrections were identified from direct radiometric tests, independent of aerosol-retrieval-related
431 considerations. The ~6% improvement in MISR-AERONET AOD agreement at Maritime sites
432 between Versions 12 and 22 (Figure 2) is traced primarily to these calibration corrections. The
433 gap that appears in the Row 2 plots of Figure 3 is comparable in magnitude to the remaining high

MISR AOD bias relative to AERONET that shows up at low AOD in the Row 3 difference plots of this figure, and could account statistically for much or all of it.

There are relatively few coincident, over-water MISR-AERONET retrievals in our data set, due to the small number of AERONET island sites, frequent cloud cover over open ocean, and silt or pollution in surface waters along many coasts that makes them unsuitable for dark water retrievals. However, over ocean, scene conditions are typically more uniform than over land, so it is easier to identify small artifacts in the retrieved values. In the much larger coincident MISR-MODIS over-ocean data set used by *Kahn et al.* [2009, Figure 5], MISR V22 AOD values, especially below about 0.25, show AOD quantization noise in approximately 0.025 increments, in addition to the gap near zero AOD. These low-AOD features are artifacts of the MISR V22 retrieval algorithm, which interpolates AOD values from a grid with 0.025 spacing.

Near coasts, where pollution, runoff, or ocean biological activity can at times significantly increase surface water reflectivity, MISR AOD can be skewed high, because the MISR over-water algorithm assumes the ocean surface is dark in the red and NIR spectral bands [e.g., Section 3.1 of *Kahn et al.,* 2007]. Figure 4 takes a closer look at MISR-AERONET coincidences over water, focusing exclusively on retrievals done with the MISR over-water algorithm, and including AOD observations coincident with the AERONET Marine Aerosol Network (MAN) [*Smirnov et al.*, 2009] as well as island stations. The vast majority of the 282 island + 61 MAN stations show very low AOD. They fall within 0.05 of the red center line, offset by +0.025, as expected based on the earlier analysis, and scatter uniformly about this line.

The outliers in Figure 4 include twelve scenes dominated by broken cloud or dust plumes, identified based on visual inspection of the image data, and marked with plus symbols; in these cases, cloud contamination or scene variability are likely factors contributing to the observed discrepancies. Data from two AERONET stations in the shallow, polluted waters of the Arabian Gulf not included in the general MISR-AERONET coincidence data set of this paper (Table 1), are highlighted with orange exes. For this population of 63 points, the MISR values tend to be skewed high relative to AERONET, as well as to the +0.025 line. Most cases unaffected by surface pollution or scene variability, for which AERONET AOD is greater than about 0.5, fall below the zero difference line, as observed in the over-land categories, but sampling is too poor to draw strong conclusions. MISR AOD behavior in coastal regions is discussed further in Section 3.4 below.

3.2. AOD Performance at Biomass Burning Sites

Focusing specifically on the Biomass Burning category, the MISR mean AOD is well within the envelopes described above, with 76% of cases falling within 0.05 or 20% × AOD of the near-coincident AERONET values, and 55% within 0.03 or 10% × AOD (Figure 2 and Table 5). These statistics cover all months of the year, whereas for most Biomass Burning sites, actual burning occurs only during a specific season, so the plots include both periods when small-medium, spherical, smoke particles dominate the aerosol load, and times when background particles prevail.

Seasonal information is given by the colors in Figure 3; summer and autumn burning season events occurring in much of the northern hemisphere appear in green and orange, respectively. Where deviations occur, especially for AOD > 0.2, the MISR value tends to be skewed low relative to AERONET (lower left panel of Figure 3). The same pattern was observed at biomass burning sites in Paper 1, as well as for specific biomass burning events by *Chen et al.* [2008], and for pollution aerosols in East Asia and at the eastern end of the Indo-Gangetic plain [Figure 6 of *Kahn et al.,* 2009]. The AOD underestimation was traced in those studies to a lack of mixtures containing spherical particles having sufficiently low SSA in the MISR Standard algorithm. This interpretation is supported by comparisons between MISR and AERONET-retrieved SSA discussed in Section 4.3 below; if aerosol SSA adopted by the MISR algorithm is too high, fewer particles are required to produce the scattered-light signal observed, and the retrieved AOD will be skewed low. In nearly two-thirds of the 68 outliers where the MISR AOD is less than 60% of the AERONET value, dark particles, either biomass burning or urban pollution, are expected. For a few of these events, for example, at Arica, Yulin, and Ispra, the AERONET-retrieved SSA is both reliable (i.e., the AERONET 440 nm AOD > 0.4) and substantially lower than the SSA obtained from the corresponding MISR retrieval. And for many others, the scene is hazy and the surrounding MISR retrieval regions produce higher AOD, conditions typical of smoke and urban pollution plumes.

As noted in the publications cited above, the MISR V22 algorithm climatology includes only one size of spherical particles having SSA other than unity (Table 2), and the algorithm is forced to select among the available choices for particle size and/or SSA. However, there are events where

the MISR-retrieved AOD is substantially lower than the corresponding AERONET value and the actual particle SSA is at or very near unity, especially for non-biomass-burning cases where AOD>~0.5 (Figure 3, bottom row of plots); such situations, where SSA is not a leading factor in AOD underestimation, are discussed in the next section.

3.3. AOD Performance at Dusty, Continental, Urban and Hybrid (smoke + dust) Sites

Statistical AOD comparisons with AERONET at Dusty sites (Figure 2 and Table 5) yield results similar to those of previous studies [*Martonchik et al.*, 2004; *Kahn et al.* 2005; *Kalashnikova and Kahn,* 2006]. AOD discrepancies with ground truth are somewhat larger over bright desert surfaces than for other site categories, but the patterns of overall agreement, some over-estimation for very low AOD and under-estimation at high AOD, as shown in Figure 3, parallel those for the Biomass Burning sites discussed above. As the details of AOD retrieval success depend in part on the aerosol optical properties included in the algorithm, some limitations in the V22 component and mixture assumptions that can affect AOD results, such as those for dusty situations, are discussed further in Section 4 below.

For Continental sites, Figure 2 and Table 5 show large differences from site to site in the level of AOD agreement between MISR and AERONET. This reflects the diversity of conditions in the Continental grouping; the sites cover an enormous range of surface fractional vegetation cover, and locations where different mixtures of spherical and non-spherical aerosols dominate. From Figure 3, there are relatively few Continental cases for which mid-visible AOD exceeds about 0.6, because these sites tend to be away from sources that produce concentrated aerosol plumes. Again the patterns of overall AOD agreement, over-estimation for very low AOD and under-estimation for AOD about 0.4 and higher (Figure 3, Row 3), parallel those for other categories. However, unlike the smoke particles discussed in Section 3.2, Continental aerosols often have SSA at or near unity, so at least one factor in addition to SSA must contribute to the observed under-estimation at high AOD.

As discussed in *Chen et al.* [2008], at higher AOD, there is less signal from the surface, and under such circumstances, the lack of surface information creates ambiguity that can result in the algorithm assigning too much of the TOA radiance to the surface (i.e., a higher surface albedo), thereby underestimating AOD. But in principle, the surface reflectance adopted by the algorithm should matter less as AOD increases, and the algorithm might partition the radiance in various

ways when there is less information about the surface. However, variations in the AOD itself can produce scene variability that could be interpreted by the MISR over-land algorithm as coming from the surface, leading to errors in the retrieved AOD in some situations.

AOD for the Continental category overall varies much less systematically with season than for the Biomass Burning and Dusty categories, due in part to greater site-to-site variability of aerosol source types for Continental cases, as well as the inherently seasonal nature of dust storm and fire occurrence. This seasonal behavior is not shown explicitly in the plots, but it is suggested by the degree to which the seasonal color-coding is more stratified for the Dusty and Biomass Burning categories in Figure 3 than for Continental cases.

MISR-AERONET AOD agreement for Urban sites in Figure 2 is similar to that for the Continental category, but the aerosol is more spatially localized. This favors MISR Central retrieval regions, compared to MISR Surrounding regions, as discussed at the beginning of Section 3; it also leads to more frequent mid-visible AOD values exceeding 0.6, as shown in Figure 3.

MISR AOD retrieval performance for the Hybrid aerosol air mass category was identified as problematic in earlier comparisons between MISR and AERONET [Paper 1] and between MISR and MODIS, especially in sub-Saharan Africa, in southern Africa, and near Mexico City during certain seasons [*Kahn et al.,* 2009]. Detailed analysis of individual cases by *Chen et al.* [2008] showed that seasonal mixing of spherical, absorbing smoke and non-spherical dust is common in western Africa from December through March. In Figure 2 of the current study, the MISR AOD retrievals in the Hybrid category again show the poorest statistical agreement with AERONET among the categories identified here. Taken together, these results reinforce the need to add mixtures of non-spherical dust with spherical, absorbing smoke particle analogs to the MISR Standard retrieval climatology. Returning to Figure 3, the qualitative trends are similar to those observed for the other categories: where outliers occur, the MISR V22 product tends to overestimate low-AOD values and underestimate high-AOD values.

3.4. Global Distribution of AOD Outliers

On a global basis, AERONET site distribution does not provide an adequate statistical assessment of AOD outlier geographical patterns; however, comparisons between coincident

MISR and MODIS/Terra AOD retrievals offer some useful insights in this regard [e.g., *Kahn et al.,* 2009]. Figure 5 shows the geographical distributions of points for which the MISR-MODIS mid-visible AOD discrepancies exceed 0.2 over land, and 0.125 over ocean, for January and July 2006. These outlier subsets represent 1% and 0.6% of the total population of coincidences over water for January and July 2006, respectively, and 10% and 6% for January and July 2006 over land. Below we associate observed outlier patterns with algorithmic factors that are likely to be involved. But aside from algorithm issues, actual differences in MISR-MODIS sampling, convolved with AOD variability at kilometer scales, contribute to the outlier populations as well, especially in high-AOD situations [e.g. *Kahn et al.,* 2007a], and even in regions of outlier concentration, only a small fraction of coincident retrievals show large discrepancies.

Regionally, the outliers tend to cluster in places where known issues occur, as discussed in *Kahn et al.* [2009]. Over land, the Sahel region of Africa stands out, as smoke and dust particles are mixed in the atmospheric column. MODIS aerosol optical models applied in this season and region include mixtures of smoke and dust particles [*Remer et al.,* 2005; *Levy et al.,* 2007], whereas the V22 MISR aerosol models do not. Generally, MISR AOD exceeds MODIS in these cases, as is indicated by the difference-plot insets of Figures 5a and 5b. For eastern China, and for northern India in January, low-SSA pollution particles are common. The MISR AOD underestimation at high AOD noted in Section 3.2 and 3.3 above, and the lack of retrieved low-SSA spherical particles in the MISR V22 product, combine to produce some of the largest outliers in the over-land data in these regions, with MISR AOD less than MODIS. In July, wildfire smoke in Siberia and parts of the western US produces similar effects, whereas smoke is sometimes mixed with dust over central Africa, so MISR-MODIS difference outliers of either sign occur in this region, though at high AOD, MISR underestimation tends to dominate. MODIS AOD overestimation over the bright land surfaces produces outliers for Patagonia in January, and this effect along with MISR AOD underestimation at high AOD generates scattered outliers in the western and central US and Europe, especially in July.

Over water, cloudy regions in the seasonal storm track bands produce most of the observed AOD differences; these appear preferentially in the Southern Ocean and across the northern mid-latitude oceans in January, and in the southern mid-latitude oceans in July. Also in July, MISR-MODIS over-water AOD differences of either sign occur where cloud and some sea-ice appear, at high northern latitudes; most often, MODIS is higher than MISR. MODIS AOD also tends to exceed MISR off the coast of west Africa in January, and off the central African coast in July,

603 places where high AOD dust or smoke plumes, or smoke-dust mixtures, are common in these
604 seasons.
605
606 There is also a concentration of outliers of either sign in some coastal regions, such as along
607 south Asia, the Red Sea, and the Arabian Gulf, especially in January. These regions correspond
608 with relatively high concentrations of dissolved organic matter in the SeaWiFS satellite ocean
609 color data (not shown). As mentioned in Section 3.1 above, the MISR and MODIS over-water
610 algorithms assume a dark ocean surface at red and longer wavelengths; *Kahn et al.* [2007a]
611 describe differences in the way these algorithms treat observed radiances in such situations that
612 can account for the retrieved AOD discrepancies. Bright coastal (Case 2) water also contributes
613 to, and in places might dominate, situations where over-water MISR and/or MODIS AOD
614 retrievals are discontinuously higher than the corresponding results for nearby land.
615

616 4. Particle Microphysical Property Retrieval Assessment

617
618 Figure 6 offers a qualitative overview of MISR aerosol-air-mass-type identification, based on the
619 lowest residual mixtures retrieved for cases where AOD > 0.15. For situations where dust is
620 most likely, mixtures containing non-spherical particles are especially common (Mixtures #51-
621 74, see Table 3). Where biomass burning smoke or urban pollution aerosol is expected, the
622 retrievals tend to pick mixtures containing spherical, absorbing particles (Mixtures #31-50). At
623 some Maritime sites, transported dust or smoke is observed, though sampling in this category is
624 poor in the MISR-AERONET coincident data, as discussed in Section 3.1 above. Spherical
625 absorbing and non-absorbing particles, as well as non-spherical dust are all common at
626 Continental, Urban, and Hybrid sites, but absorbing particles appear less frequently at
627 Continental than at Urban and Hybrid sites, where aerosol containing black carbon from
628 incomplete combustion is more likely to be found.
629
630 Figure 7 presents a geographically oriented view of retrieved aerosol properties, in the same
631 three broad categories highlighted in Figure 6: Spherical Non-absorbing (cyan), Spherical
632 Absorbing (magenta), and Non-spherical (yellow), from the July 2007 MISR V22 aerosol
633 product. The MISR algorithm *retrieves* aerosol properties from a climatology of components
634 and mixtures that is applied globally (Tables 2 and 3), rather than pre-selecting them based on
635 region or season. Many expected patterns appear, such as non-spherical dust analogs over and

636 downwind of North African and Middle Eastern desert dust sources. Spherical, absorbing smoke
637 analogs are retrieved in tropical and boreal summertime biomass burning regions, and similar
638 particle types are found around pollution centers along the east coasts of North America and
639 China, whereas spherical, non-absorbing maritime particles are retrieved over much of the
640 Southern Hemisphere oceans.
641
642 Some artifacts appear as well, especially in remote-ocean and other low-AOD regions where
643 sensitivity to particle properties is reduced. Non-spherical particles are retrieved at times over
644 equatorial, southern hemisphere and some boreal waters that are likely to be unscreened cirrus
645 [*Pierce et al.,* 2010]. Absorbing, spherical particles are frequently retrieved over northern
646 hemisphere oceans in the July map, and shift to the southern hemisphere oceans for January 2007
647 (not shown). In these regions, the range of scattering angles viewed by MISR, and hence the
648 sensitivity to particle type, is limited in summer [Figure 2 of *Kahn et al.,* 1997].
649
650 **4.1. Angstrom Exponent (ANG)**
651
652 In this section, we go beyond the broad, qualitative assessments, by comparing MISR and
653 AERONET ANG differences as a function of AERONET AOD, for Biomass Burning, Dusty,
654 and Continental sites, stratified by season (Figure 8). The difference plots provide a more
655 sensitive representation of deviations than the scatter plots that are often used for such
656 comparisons. Smaller dots identify cases where AOD is below 0.15, and arrows highlight some
657 of the low-AOD situations where the MISR ANG values are especially scattered, relative to
658 AERONET. As has been discussed in previous papers (e.g., Paper 1), this is expected; particle
659 microphysical property information is reduced when the AOD is below about 0.15 or 0.2,
660 depending on conditions, due to increased relative contributions from surface reflectance
661 uncertainties, unmasked cloud, etc. However, as a consequence of the systematic air mass factor
662 sampling MISR multi-angle views provide, MISR AOD retrievals themselves tend to be robust
663 down to values of 0.05 or lower even when particle microphysical properties are poorly
664 constrained [e.g., *Kahn et al.*, 1998; Paper 1].
665
666 Most of the biomass burning cases in this dataset occur during northern summer and autumn. As
667 Panels c and d in Figure 8 illustrate, the MISR-retrieved ANG values scatter fairly uniformly
668 around the zero-difference line during these seasons; there is good statistical agreement between
669 MISR and AERONET ANG for biomass burning situations when AOD > 0.15. However, as

noted above, the range of spherical particle size and SSA combinations in the V22 retrieval algorithm is limited, so a richer set of components and mixtures would reduce the observed scatter. This has been demonstrated with the MISR Research Aerosol retrieval algorithm for individual cases [e.g., *Chen et al.*, 2008], but for implementation in the Standard algorithm, accommodation must also be made for situations where particle property information in the observations is limited (see Section 5). Figure 8e displays the MISR-AERONET ANG difference as a function of AERONET ANG for Biomass Burning sites. Although the vast majority of points in this panel are over-plotted close to the zero-ANG-difference line (easier to see from panels a-d), the outliers show a tendency for MISR to overestimate ANG when the AERONET ground-truth ANG value is small, and conversely, to underestimate ANG when it is large. That is, the dynamic range of MISR-retrieved ANG is less than that of AERONET, further indicating that a richer set of spherical components and mixtures could improve the results.

Dust events in this data set are most common during northern spring and summer. Panels g and h of Figure 8 show that the MISR V22 algorithm systematically overestimates ANG at sites frequently dominated by desert dust when AOD > 0.15, indicating that the particles retrieved by MISR under dusty conditions tend to be smaller than those observed by AERONET. Figure 8j illustrates more specifically that when AERONET ANG < 1 (indicating that medium-to-large particles dominate), MISR retrieves smaller particles (larger ANG). Several factors likely contribute to this trend. The MISR algorithm contains only two non-spherical components, one medium and one coarse-mode aerosol analog (Table 2); the coarse-mode optical model, generated from a distribution of ellipsoids, does not provide a completely satisfactory match to thick, near-source dust plumes observed by MISR, even when combined with medium-mode dust [*Kalashnikova and Kahn,* 2006]. Developing more generally applicable coarse-mode dust optical models is the subject of current research [e.g., *Bi et al.*, 2010]. In addition, due to a lack of spectral channels longer than 866 nm, MISR is insensitive to the optical properties of coarse-mode particles larger than about 2.5 μm diameter, whereas desert dust aerosol distributions often contain a significant fraction of particles up to about 10 μm in size, especially near sources.

According to Figure 8, there is also a tendency for the MISR retrievals to overestimate ANG at Continental sites, and the ANG dynamic range is again smaller than that obtained by AERONET (Figure 8o), further indicating the need for a richer set of components and mixtures in the

retrieval climatology. In particular, the effective radius of the "large spherical" particle among the V22 aerosol components is 2.80 μm (Particle #6 in Table 2), and the next-smaller spherical particles are 0.26 and 0.12 μm in size (Particles #3 and #2, respectively). Absorbing spherical particles are available only at 0.12 μm effective radius in V22 (Particles #8 and #14). Given the limited mixtures available in V22, for situations where the retrieved ANG is too high, the MISR algorithm often picks a combination of unduly small particles, along with enough very large particles to match the observed radiances as much as possible.

Field data indicate that particles of sizes intermediate between Particles #3 and #6 are significant in some regions. The AERONET climatology is dominated by a "Fine Mode" component having very nearly the size distribution of Particle #2 (Table 2) for all aerosol type categories, and a "Coarse Mode" component that is much more variable, but with a mid-range close to MISR Particle #6 [*Dubovik et al.*, 2002; to compare this reference with Table 2 here, the AERONET particle size parameters were converted from volume-weighted to number-weighted log-normal distribution values]. However, even though the AERONET data are often interpreted in terms of bi-modal distributions by fitting their 22 size bins with two log-normal distributions, an additional medium mode appears in the underlying retrievals in some cases, for example at Cape Verde, the Maldives, and possibly Bahrain in *Dubovik et al.* [2002, Figure 1] based on AERONET Version 1 processing, and at Ilorin in west Africa [*Eck et al.*, 2010] with the more robust Version 2 processing. More generally, spherical particles having sizes between the 0.26 and 2.80 μm V22 MISR components can form as pollution and biomass burning particles age, for example, downwind of the east coasts of North America and China. These regions are not well sampled by AERONET stations, but contribute significantly to satellite data records having global coverage.

4.2. Constraints on Particle Size as a Categorical Variable

Spherical-particle sensitivity studies using a fine grid of spherical particle sizes and SSA values indicate that in general, MISR can separate three-to-five size groupings under good retrieval conditions, i.e., when mid-visible AOD $\gtrsim$ 0.15 or 0.2, with minimal cloud, surface snow and ice, or whitecap contamination, and for relatively uniform aerosol loading on 1 to 10 km scales [*Chen et al.,* 2008; *Kahn et al.*, 1998]. As such, a size range intermediate between the "coarse" and "fine" modes, discussed in Section 4.1 above, can be distinguished from the MISR data. The

sensitivity studies also showed that particle size, as retrieved by MISR, should be treated as a categorical rather than a continuous variable, providing an aerosol type *classification* amounting to "small," "medium," and "large."

This classification is reflected in the MISR aerosol product variable Regional Best-Estimate Spectral Optical Depth Fraction (RegBestEstimateSpectralOptDepthFraction), which reports the fraction of total column AOD assigned to particles having radius <0.35 μm (small), 0.35 to 0.70 μm (medium), and > 0.70 μm (large). The classification is based upon the sensitivity studies cited above, and on the Version 12 algorithm, which included intermediate-sized particles having effective radius 0.57 and 1.28 μm [Paper 1].

To assess MISR-retrieved particle size as a categorical variable, we applied k-means cluster analysis to the MISR vs. AERONET ANG values. The AERONET ANG values are obtained from direct-sun measurements and provide a reliable and well-sampled ground-truth quantity (see Section 2.1 above), whereas AERONET size distributions are derived with additional assumptions. We subsequently interpret the comparative ANG values in terms of the MISR-retrieved mixtures and components.

The clustering approach determines bins or "clusters" directly from the data, rather than imposing them arbitrarily, as must be done, e.g., for 2-d histograms. The algorithm used begins with k "seeds," constituting an initial guess at the number and centroid values of the clusters. Using a distance metric, the algorithm identifies all points that are closer to a given seed than any other, and calculates the centroid of all points associated with each seed. These centroids are then taken as the new seeds, and the process is iterated until convergence [e.g., *Press et al.,* 2007]. This approach allows us to determine the number and range of ANG classes in the data, and to evaluate their degree of separation. The number of categories that the data can distinguish is obtained as the highest value of k that produces separable clusters arrayed near the 1:1 line in a plot of retrieved vs. validation ANG data. We used simple Euclidean distance as our metric, and performed the cluster analysis for k values of 2, 3, 4, and 5 on the coincident MISR-AERONET ANG pairs for each of the six aerosol type categories. Several initial seed locations were tested in each case, to assure the robustness of the results.

768 The plots in Row 1 of Figure 9 show the results for k=3, i.e., the algorithm was initiated with
769 three cluster seeds, which are marked as open black circles. The centroids of the final clusters,
770 shown as solid black circles in these plots, are systematic, and fall roughly along the 1:1 line for
771 the Maritime category. For the Urban, Continental, Hybrid, and Biomass Burning classes, two
772 of the three point clouds are less separable when projected along the vertical (MISR ANG) axis.
773 The clusters are more systematic for k=2, and become increasingly scattered when k=4 and 5
774 (not shown). To help interpret these results in terms of what they say about the particle types
775 available in the V22 algorithm, Figure 9 also shows, in Row 2, scatter plots of AOD (similar
776 format to Figure 3), and in Rows 3-5, histograms of all successful mixtures in the retrievals
777 (similar format to Figure 6) for each of the three clusters, respectively. These plots are color-
778 coded by the clusters identified in the Row 1 plots. As expected, the large particle clusters
779 (green; small ANG) are associated with systematically higher AOD for the Dusty and Hybrid
780 categories shown in Row 2, whereas the small and medium particle clusters (orange and purple)
781 tend to have higher AOD for sites often dominated by Biomass Burning smoke; the situation for
782 Continental and Urban sites is more mixed.
783
784 The Figure 9 data confirm, and add specificity to, many expected patterns in particle size, and
785 more generally, in particle type (e.g., Figure 7). In Figure 9 Row 3, the preponderance of small,
786 absorbing smoke particles stands out (Mixtures #31-36 and 41-45; Table 3) in the Biomass
787 Burning and Hybrid categories, and their occurrence at times in the other categories is also
788 evident. Spherical non-absorbing particles are common in all categories, especially Mixtures
789 #11-18, containing the small-medium particle (0.12 μm effective radius) that is also the fine-
790 mode size distribution preferred by AERONET; it is mixed with up to 60% mid-visible AOD of
791 the very large spherical component (Particle #6), the common coarse-mode component of the
792 AERONET climatology. In the Dusty and Hybrid categories, mixtures containing fine-mode
793 spherical-absorbing particles along with significant fractions of the very large, spherical Particle
794 #6 are also common.
795
796 Considering next the low-ANG, larger-effective-particle-size clusters represented in Rows 4 and
797 5, the peaks progressively broaden in all categories except Dusty, moving toward greater
798 admixtures of the very large, spherical particles within each 10-mixture grouping of the MISR
799 algorithm climatology (Table 3), as would be expected. Medium dust is more common, and
800 coarse dust (Mixtures #63-74), which is nearly absent from the Row 3 clusters, makes significant
801 contributions to most categories. Note that for the Continental and Urban categories, the

802 respective mixture spectra in Rows 4 and 5 are very similar for all mixture groupings, and for
803 Biomass Burning, the main difference is a shift between small, spherical particles having
804 different SSA values. This demonstrates why the purple and green (medium and small ANG)
805 clusters for these categories in Row 1 have poorly resolved ANG values in the MISR data,
806 despite having significantly different values in the AERONET data. Field-measured size
807 distributions and previous MISR sensitivity studies suggest that adding to the mixtures in Table
808 3 components intermediate in size between the small-medium spherical Particle #3 and the very
809 large spherical Particle #6, should move the centroids of the green clusters toward smaller ANG,
810 achieving closer agreement with the AERONET ANG ground-truth. The same would also
811 apply to the Biomass Burning and Hybrid categories, except that here, absorbing particles larger
812 than 0.12 μm effective radius would be needed [*Chen et al.,* 2008].
813
814 The situation with the Dusty category is more complex. The MISR ANG corresponding to the
815 highest AERONET ANG values are too small; there are not adequate mixtures of dust with a
816 medium-mode spherical particle, so mixtures of medium dust with the large spherical Particle
817 #6, and mixtures of small absorbing (especially Row 4) and non-absorbing (especially Row 5)
818 spherical particles with Particle #6 are often selected. In part, Particle #6 is substituting for dust,
819 as there are few alternative mixture options in the V22 climatology, and in addition, the current
820 coarse-mode dust optical model does not match the MISR data well [*Kalashnikova and Kahn*,
821 2006].
822
823 In summary, AERONET provides a powerful tool for validating ANG. When sufficient
824 component and mixture options are available, the MISR algorithm distinguishes at least three
825 groupings in ANG, but detailed analysis also highlights specific limitations in the current
826 component and mixture tables, and in particular, a lack of medium-mode particles.
827
828 **4.3. Particle Single-scattering Albedo (SSA) and Particle Sphericity**
829
830 For MISR, particle SSA and shape are also categorical variables; sensitivity analyses and early
831 validation studies indicate two-to-four groupings in SSA, and at least spherical vs. non-spherical
832 shape, can be distinguished under good retrieval conditions (as defined in Section 4.2) [*Chen et*
833 *al.,* 2008; *Kalashnikova and Kahn*, 2006; *Kahn et al.,* 1997; 1998].
834

We attempted to validate MISR-retrieved SSA with AERONET, but there were too few coincident events meeting the AERONET high AOD and low solar elevation angle acceptance criteria to obtain a statistical sampling of SSA retrievals. The cases obtained are not representative of average conditions, though AERONET SSA values in general provide the most extensive suborbital coverage available.

Qualitatively, MISR tends to obtain SSA at or near unity, especially when the AOD is too low for MISR to produce good SSA constraints. Globally, sea salt and sulfate aerosols are non-absorbing, and in addition, aged smoke and some pollution particles are only weakly absorbing, so this is a reasonable value to adopt in these circumstances. As discussed earlier, MISR does tend to retrieve absorbing particles preferentially at Biomass Burning and Hybrid sites in seasons when smoke is expected (Figures 6 and 7).

Even with the limited particle component and mixture options available in V22, MISR-retrieved SSA helps distinguishing aerosol air mass types, especially when combined with retrieved particle size and/or shape information, as demonstrated statistically at the beginning of Section 4, and in available field campaign events where coincident suborbital measurements of the key validation quantities were made [e.g., Figure 6 of *Kahn et al.,* 2008].

Validating MISR-retrieved particle shape is also challenging, again because ground truth is difficult to obtain. Although information about particle sphericity can be derived from AERONET sky-scan data [*Dubovik et al.*, 2006], non-spherical AOD fraction is not yet provided as a validated field in the AERONET products. Individual cases where other coincident aircraft or surface field observations were obtained provide some additional tests of the retrieval results [e.g., *Kalashnikova and Kahn,* 2006; *Kahn et al.,* 2008; *Schladits et al.,* 2008], and the evolution of the MISR-retrieved fraction AOD spherical for dust plumes during transport over ocean follows expected patterns [*Kalashnikova and Kahn,* 2008]. MISR-retrieved particle shape also helps distinguish dust from spherical particles for air quality applications [*Liu et al.,* 2007a; b], contributes to mapping changes in the seasonal distribution of anthropogenic vs. natural aerosols over India [*Dey and Di Girolamo, 2010*], and discriminates between thin cirrus, spherical particles, and to some extent dust, over ocean [*Pierce et al.,* 2010]. In each of these studies, further validation of the MISR-retrieved particle properties specific to the application was performed, offering qualitative support for the MISR particle sphericity retrieval results, as do Figures 6 and 7 of the current paper, discussed above.

5. Summary of Recommendations

The data set developed and analyzed in this paper adds to earlier product validation statistical comparisons having smaller samplings, and to field campaign and other case studies. The effort has allowed us to take a detailed and critical look at the MISR V22 aerosol products, with the aim of assessing strengths and identifying specific areas where further improvements are possible. In this section, we summarize the issues identified, and suggest ways of addressing some of them in future aerosol product versions. Bear in mind that most of these issues affect small fractions of the data set and are confined to specific retrieval situations, geographic regions, and in some cases seasons. Overall AOD performance, in global context, is summarized in the Conclusions section, which follows.

• There is a *gap in MISR-retrieved mid-visible AOD values below about 0.02*, as well as *quantization noise at 0.025 AOD intervals* reported previously from MISR-MODIS AOD comparisons. The gap tends to skew the retrieved AOD to higher values, and is especially significant statistically for very low-AOD situations that dominate the Maritime category. This is also likely to contribute to adjacent land-ocean AOD differences, which tend to show higher AOD over ocean in some regions. The numerical scheme in future versions of the algorithm will correct these issues.

• There is a *lack of medium spherical particles* in the V22 climatology, having effective radii between 0.26 and 2.8 μm. This tends to skew the retrieved ANG to larger values (smaller particles) in some situations. Based on field observations, the addition of mixtures containing spherical non-absorbing and also weakly absorbing (mid-visible SSA ~ 0.94) particles having effective radius around 0.57 μm, and also a spherical non-absorbing component at about 1.25 μm, should address this issue at the level-of-detail appropriate to typical MISR sensitivity.

• There is a *lack of spherical, absorbing particles* in the V22 climatology at sizes other than 0.12 μm effective radius. This tends to skew the retrieved AOD to lower values when absorbing spherical particles are present, as the algorithm sometimes selects spherical non-absorbing particles closer to the AERONET-observed size range. The issue is most common for the

902 Biomass Burning and Urban categories. Based on field measurements, the addition of spherical
903 absorbing and weakly absorbing particles (mid-visible SSA around 0.84 and 0.94, respectively)
904 having effective radius around 0.06 μm, and weakly absorbing particles having effective radius
905 around 0.26 μm, should address this issue [e.g., *Chen et al.,* 2008; *Dubovik et al.,* 2002].
906 Adjusting the SSA of the spherical absorbing and weakly absorbing 0.12 μm particles in the
907 current algorithm (Table 2) to these values could also improve the situation. The spectral
908 dependence of SSA represents an additional dimension to be considered, as Urban Pollution
909 particles have generally shallower spectral slope than Biomass Burning particles [e.g., *Bond and*
910 Bergstrom, 2006; *Chen et al.,* 2008; *Reid et al.,* 2005].
911
912 • For AERONET *AOD >~ 0.4, MISR-retrieved AOD is frequently underestimated* over land
913 (Figure 3), and possibly also over water, though sampling over dark, cloud-free water is too
914 small to draw a strong conclusion (Figure 4). Several factors appear to be involved. (1) In
915 situations where the atmospheric particles are absorbing, MISR tends to adopt an SSA at or near
916 unity due to a lack of absorbing, spherical particles in the V22 climatology. This skews the
917 retrieved AOD low [*Kahn et al.,* 2005a; 2007; *Chen et al.,* 2008]. (2) Most high-AOD
918 underestimation cases occur when the actual particle SSA is at or near unity, so MISR SSA
919 overestimation is not a factor. As the MISR over-land algorithm assumes that TOA reflectance
920 variability on one-to-ten-kilometer scales comes entirely from the surface, AOD variability on
921 these scales could be assigned to the surface, causing an AOD underestimation. Unlike surface
922 reflectance variability, the contributions of aerosol variations to the scene tend to increase with
923 increasing view angle. This could be used to identify and flag such situations. Similarly, testing
924 whether the MISR-retrieved surface angular reflection factors differ significantly from location-
925 specific values in a climatology derived from low-AOD MISR observations could be used for
926 this purpose. (3) Other algorithmic factors are also under investigation by the MISR team.
927
928 • There is a *lack of mixtures containing both spherical, absorbing smoke analogs and non-*
929 *spherical dust* in the V22 climatology. This results in poor AOD performance for the Hybrid
930 category. Theoretical sensitivity analysis suggest that two-component mixtures in 10 or 20%
931 AOD increments would capture the information content of the MISR data under good retrieval
932 conditions [*Kahn et al.*, 2001; *Chen et al.,* 2008].
933

• In the V22 algorithm, ANG in the Dusty category tends to be over-estimated. As discussed by *Kalashnikova and Kahn* [2006], *an upgraded coarse-mode dust optical analog* should improve ANG, and to some extent AOD retrievals, when dust dominates the aerosol air mass, especially near dust source regions. The inclusion of medium-mode spherical particles in the algorithm climatology seems likely to help reduce this discrepancy too, as discussed in Section 4 above.

• In *situations where the range of scattering angles observed by MISR is diminished* by solar geometry and sun-glint over water, and/or when mid-visible AOD is below about 0.15 or 0.2, particle property information is diminished, and absorbing spherical particles are sometimes retrieved where none are expected. Flagging cases having low AOD or limited scattering angle coverage, or more generally, when many mixtures pass the algorithm acceptance criteria, would alert users to the possibility that particle property information in the observations is limited. Similarly, *coastal water sites, where seasonally high runoff or ocean biological activity can increase ocean surface reflectance*, and other regions and seasons where algorithm assumptions tend to be violated (Figure 5), can be flagged as a warning that retrieved AOD might be aliased.

6. Conclusions

We have assessed the MISR V22 AOD and ANG products with coincident AERONET sun photometer observations from around the globe, and have examined qualitatively MISR-retrieved SSA and fraction AOD spherical. Comparisons were stratified by season and by location; AERONET sites having good measurement records over the MISR observing period were partitioned into six categories, based on expected aerosol air mass type. One challenge facing the validation effort, and the interpretation of MISR (and other) remote-sensing products, is that retrieval sensitivity varies considerably depending upon environmental conditions, which include AOD, surface brightness, scene heterogeneity, range of scattering angles observed, and actual aerosol components in the column. The variation in sensitivity to particle properties has implications for the retrieval algorithm itself; the range of aerosol components and mixtures selected for the retrieval climatology represents a compromise between conciseness, to limit redundancy and reduce algorithm run time, and completeness, to capture the information content of the measurements under the best observing conditions.

967 Overall, about 70% to 75% of MISR AOD retrievals fall within 0.05 or 20% × AOD of the
968 paired validation data, and about 50% to 55% meet the 0.03 or 10% × AOD criterion, except in
969 the Dusty and Hybrid (smoke + dust) categories. Substantially improved agreement compared to
970 the early post-launch assessment [*Kahn et al.*, 2005a] was achieved for the Maritime and
971 Biomass Burning categories (Figure 2), mostly due to calibration adjustments and the addition of
972 spherical absorbing aerosol components, respectively, made after the 2005 assessment.
973
974 Scene heterogeneity makes an important contribution to MISR-AERONET AOD discrepancies.
975 Sampling differences rather than retrieval error contribute to over 80% of significant outliers in
976 the paired MISR-AERONET data set (3.7% of all coincident cases). For the Maritime,
977 Continental, and Dusty categories, averaging MISR retrievals covering a ~50 km spatial scale
978 provides systematically better agreement with the AERONET ±1 hour time-series than
979 comparing with only the central 17.6 km MISR retrieval region containing the AERONET site.
980 For the Urban category, persistent small-spatial-scale variability produces a statistical advantage
981 when only the central MISR retrieval region is considered. As expected, the largest seasonal
982 variability was found at most sites designated Biomass Burning or Dusty.
983
984 AERONET also provides powerful validation for ANG from direct-sun measurements at
985 multiple wavelengths. When sufficient component and mixture options are available, the MISR
986 algorithm distinguishes three-to-five groupings in ANG, based on sensitivity analysis and case
987 studies for which we have validation data. The MISR V22 product distinguishes two or three size
988 bins, depending on aerosol type, as well as spherical vs. non-spherical particles, and in some
989 circumstances, about two bins in SSA. But unlike the situation for AOD and ANG, there is too
990 little MISR-AERONET coincident validation data for SSA and particle shape to perform formal
991 statistical assessments. To some extent, expected trends in particle absorption properties and
992 non-spherical AOD fraction are observed, and qualitative assessment is supplemented by
993 previously published case studies for which near-coincident field observations were obtained
994 [e.g., *Kahn et al.,* 2004; 2008; *Redemann et al.,* 2005; *Reidmiller et al.,* 2006; *Schmid et al.,*
995 2003]. Based on the validation study results, specific algorithm upgrades are proposed, and are
996 summarized in Section 5 above; the MISR team is addressing each of them, such as
997 modifications to the component particle optical models and mixtures to maximize particle type
998 discrimination.
999

This paper provides formal validation of the MISR V22 aerosol product. As with any remote sensing measurements, there are strengths and limitations. Here we have identified the key issues and traced them to specific retrieval conditions, information essential for applying and interpreting the data appropriately. Care must be taken with MISR AOD values at the extremes, when mid-visible AOD is likely to be > 0.5 and when it is expected to be very small (< 0.025). The impact on retrieved AOD of variability, especially within aerosol plumes, of bright water surfaces, and broken cloud situations, should also be considered. Sensitivity to particle microphysical properties is diminished for mid-visible AOD below about 0.15 or 0.2.

Taking these caveats into account, MISR-retrieved AOD over water, land, and bright surfaces is used to study zonal mean aerosol short-wave forcing [*Kim and Ramanathan*, 2008; *Kishcha et al.,* 2009] as well as regional long-wave forcing [*Zhang and Christopher*, 2003]. The MISR aerosol product has also been used to monitor dust plume evolution [*Kalashnikova and Kahn*, 2008] and air quality [*Liu et al.*, 2007a;b; *van Donkelaar et al.*, 2010], to map aerosol air mass type evolution [*Dey and Di Girolamo*, 2010], and to validate aerosol transport model AOD simulations. [*Yu et al.*, 2006; *Kinne et al.*, 2006]. Additional information helpful for applying the MISR aerosol product can be found in *Kahn et al.* [2009] and the MISR Data Quality Statements available online [http://eosweb.larc.nasa.gov/PRODOCS/misr/table_misr.html].

Acknowledgments

We thank our colleagues on the Jet Propulsion Laboratory's MISR instrument team and at the NASA Langley Research Center's Atmospheric Sciences Data Center for their roles in producing the MISR data sets, and Susan Paradise for contributions to Figure 4 and related discussion of over-water retrievals. We also thank the AERONET principal investigators for contributing to the global aerosol database. The work of R. Kahn is supported in part by NASA's Climate and Radiation Research and Analysis Program, under H. Maring, NASA's Atmospheric Composition Program, and the EOS-MISR project.

References

Abdou, W.A., D.J. Diner, J.V. Martonchik, C.J. Bruegge, R.A. Kahn, B.J. Gaitley, K.A. Crean, L.A. Remer, and B. Holben, 2005, Comparison of coincident MISR and MODIS aerosol optical depths over land and ocean scenes containing AERONET sites, *J. Gelphys. Res.*, doi:10.1029/2004JD004693.

Anderson, T. L., R.L. Charlson, D.M. Winker, J.A. Ogren, and K. Holmen, 2003. Mesoscale variations of tropospheric aerosols, *J. Atmosph. Sci., 60*, 119-136.

Bi, L., P. Yang, G.W. Kattawar, and R. Kahn, 2010. Modeling optical properties of mineral aerosol particles by using non-symmetric hexahedra, *Appl. Opt.* 49, 334-342.

Bond, T.C., and R.W. Bergstrom, 2006. Light absorption by carbonaceous particles: An investigative review. *Aerosol Sci. Tech*. 40:27-67.

Bruegge, C.J., D.J. Diner, R.A. Kahn, N. Chrien, M.C. Helmlinger, B.J. Gaitley, W.A. Abdou, 2007. The MISR radiometric calibration process, *Remt. Sensing Environ. 107*, 2-11, doi:10.1016/j.rse.2006.07.024.

Chen, W-T, R. Kahn, D. Nelson, K. Yau, and J. Seinfeld, 2008, Sensitivity of multi-angle imaging to optical and microphysical properties of biomass burning aerosols, *J. Geophys. Res.* 113, D10203, doi:10.1029/2007JD009414.

Chen, Y., Q. Li, R. A. Kahn, J. T. Randerson, and D. J. Diner, 2009. Quantifying aerosol direct radiative effect with Multiangle Imaging Spectroradiometer observations: Top-of-atmosphere albedo change by aerosols based on land surface types, J. Geophys. Res., 114, D02109, doi:10.1029/2008JD010754.

Christopher, S, and J. Wang, 2004. Intercomparison between multi-angle imaging spectroradiometer (MISR) and sunphotometer aerosol optical thickness in dust source regions of

China, implications for satellite aerosol retrievals and radiative forcing calculations. *Tellus,* Ser. B 56, 451-456.

Dey, S., and L. Di Girolamo, 2010. A climatology of aerosol optical and microphysical properties over the Indian subcontinent from nine years (2000-2008) of Multi-angle Imaging SpectroRadiometer (MISR) data. *J. Geophys. Res.*, in press.

Di Girolamo, L., and M.J. Wilson, 2003. A first look at band-differenced angular signatures for cloud detection from MISR. *IEEE Trans. Geosci. Remote Sens.* **41**, 1730-1734.

Diner, D.J., J.C. Beckert, T.H. Reilly, C.J. Bruegge, J.E. Conel, R. Kahn, J.V. Martonchik, T.P. Ackerman, R. Davies, S.A.W. Gerstl, H.R. Gordon, J-P. Muller, R. Myneni, R.J. Sellers, B. Pinty, and M.M. Verstraete, 1998. Multiangle Imaging SpectroRadiometer (MISR) description and experiment overview, IEEE Trans. Geosci. Remt. Sensing 36, 1072-1087.

Diner, D.J., W.A. Abdou, J.E. Conel, K.A. Crean, B.J. Gaitley, M. Helmlinger, R.A. Kahn, J.V. Martonchik and S.H. Pilorz, 2001. MISR aerosol retrievals over southern Africa during the Safari-2000 dry season campaign. *Geophys. Res. Lett.* 28, 3127-3130.

Diner, D.J., R.A. Kahn, C.J. Bruegge, J.V. Martonchik, W.A. Abdou, B.J. Gaitley, M.C. Helmlinger, O.V. Kalashnikova, and W-H. Li 2004. Refinements to MISR's radiometric calibration and implications for establishing a climate-quality aerosol observing system. Proc. SPIE 5652, 57-65.

Diner, D.J., W.A. Abdou, T.P. Ackerman, K. Crean, H.R. Gordon, R.A. Kahn, J.V. Martonchik, S.R. Paradise, B. Pinty, M.M. Verstraete, M, Wang, and R.A. West, 2006. Multi-angle Imaging SpectroRadiometer Level 2 Aerosol Retrieval Algorithm Theoretical Basis, Revision F. Jet Propulsion Laboratory, California Institute of Technology JPL D-11400.

Dubovik, O., and M.D. King, 2000. A flexible inversion algorithm for retrieval of aerosol optical properties from Sun and sky radiance measurements, J. Geophys. Res. 105, 20673-20696.

1095 Dubovik, O., A. Smirnov, B.N. Holben, M.D. King, Y.J. Kaufman, T.F. Eck, and I. Slutsker,
1096 2000. Accuracy assessments of aerosol optical properties retrieved from Aerosol Robotic
1097 Network (AERONET) Sun and sky radiance measurements, J. Geophys. Res. 105, 9791-9806.
1098
1099 Dubovik, O., B. Holben, T.F. Eck, A. Smirnov, Y.J. Kaurman, M.E. King, D. Tanre, and I.
1100 Slutsker, 2002. Variability of absorption and optical properties of key aerosol types observed in
1101 worldwide locations, J. Atmosph. Sci. 59, 590-608.
1102
1103 Dubovik, O., A. Sinyuk, T. Lapyonok, B.N. Holben, M. Mishchenko, P. Yang, T.F. Eck, H.
1104 Volten, O. Munoz, B. Viehelmann, W.J. van der Zande, J-F. Leon, M. Sorokin, And I. Slutsker,
1105 2006. Application of spheroid models to account for aerosol particle nonsphericity in remote
1106 sensing of desert dust. *J. Geophys. Res. 111*, doi:10.1029/2005JD006619.
1107
1108 Eck, T.F., B.N. Holben, J.S. Reid, O. Dubovik, A. Smirnov, N.T. O'Neill, I. Slutsker, and S.
1109 Kinne, 1999. Wavelength dependence of the optical depth of biomass burning, urban, and desert
1110 dust aerosols. *J. Geophys. Res. 104*, 31333-31349.
1111
1112 Eck, T.F., B.N. Holben, A. Siniuk, R.T. Pinker, P. Golob, H. Chen, B. Chatenet, Z. Li, R.P.
1113 Singh, S.N. Tripathi, J.S. Reid, D.M. Giles, O. Dubovik, N.T. O'Neil, and A. Smirnov, 2010.
1114 Climatological aspects of the optical properties of fine/coarse mode aerosol mixtures, *J.*
1115 *Geophys. Res., in press*.
1116
1117 Haywood, J. and M. Schulz, 2007. Causes of the reduction in uncertainty in the anthropogenic
1118 radiative forcing of climate between IPCC (2001) and IPCC (2007). *Geophys. Res. Let. 34*,
1119 L20701, doi:10.1029/2007GL030749.
1120
1121 Holben, B.N., et al., 1998. AERONET – A federated instrument network and data archive for
1122 aerosol characterization, *Remote Sens. Environ. 66*, 1-16.
1123
1124 IPCC, 2007. The Physical Science Basis. Contribution of Working Group I to the Fourth
1125 Assessment Report of the Intergovernmental Panel on Climate Change. Solomon, S., D. Qin, H.
1126 Manning, Z. Chen, M. Marquis, K. Averyt, M. Tignor, and H. Miller, eds. Cambridge University
1127 press.
1128

1129 Jiang, X., Y. Liu, B. Yu and M. Jiang, 2007. Comparison of MISR aerosol optical thickness with
1130 AERONET measurements in Beijing metropolitan area. *Rem. Sens. Environ.* 107, 45-53.
1131
1132 Kahn, R., R. West, D. McDonald, B. Rheingans, and M.I. Mishchenko, 1997. Sensitivity of
1133 Multi-angle remote sensing observations to aerosol sphericity, *J. Geophys. Res., 102*, 16861-
1134 16870.
1135
1136 Kahn, R., P. Banerjee, D. McDonald, and D. Diner, 1998. Sensitivity of Multiangle imaging to
1137 Aerosol Optical Depth, and to Pure-Particle Size Distribution and Composition Over Ocean, *J.*
1138 *Geophys. Res. 103*, 32,195-32,213.
1139
1140 Kahn, R., P. Banerjee, and D. McDonald, 2001. The Sensitivity of Multiangle Imaging to
1141 Natural Mixtures of Aerosols Over Ocean, J. Geophys. Res.106, 18219-18238.
1142
1143 Kahn, R., J. Anderson, T.L. Anderson, T. Bates, F. Brechtel, C.M. Carrico, A. Clarke, S.J.
1144 Doherty, E. Dutton, R. Flagan, R. Frouin, H. Fukushima, B. Holben, S. Howell, B. Huebert, A.
1145 Jefferson, H. Jonsson, O. Kalashnikova, J. Kim, S-W. Kim, P. Kus, W-H. Li, J.M. Livingston, C.
1146 McNaughton, J. Merrill, S. Mukai, T. Murayama, T. Nakajima, P. Quinn, J. Redemann, M.
1147 Rood, P. Russell, I. Sano, B. Schmid, J. Seinfeld, N. Sugimoto, J. Wang, E.J. Welton, J-G. Won,
1148 S-C. Yoon, Environmental Snapshots From ACE-Asia, *J. Geophys. Res.*, doi:2003jd004339,
1149 2004.
1150
1151 Kahn, R., B. Gaitley, J. Martonchik, D. Diner, K. Crean, and B. Holben, 2005a. MISR global
1152 aerosol optical depth validation based on two years of coincident AERONET observations, *J.*
1153 *Geophys. Res., doi:10:1029/2004JD004706.*
1154
1155 Kahn, R., W-H. Li, J. Martonchik, C. Bruegge, D. Diner, B. Gaitley, W. Abdou, O. Dubovik, B.
1156 Holben, S. Smirnov, Z. Jin, and D. Clark, 2005b. MISR low-light-level calibration, and
1157 implications for aerosol retrieval over dark water, *J. Atmosph, Sci.* 62, 1032-1062.
1158
1159 Kahn, R. A., M. J. Garay, D. L. Nelson, K. K. Yau, M. A. Bull, B. J. Gaitley, J. V. Martonchik,
1160 and R. C. Levy, 2007a. Satellite-derived aerosol optical depth over dark water from MISR and
1161 MODIS: Comparisons with AERONET and implications for climatological studies, J. Geophys.
1162 Res., 112, D18205, doi:10.1029/2006JD008175.

Kahn, R. A., W.-H. Li, C. Moroney, D. J. Diner, J. V. Martonchik, and E. Fishbein, 2007b. Aerosol source plume physical characteristics from space-based multiangle imaging, J. Geophys. Res., 112, D11205, doi:10.1029/2006JD007647.

Kahn, R., A. Petzold, M. Wendisch, E. Bierwirth, T. Dinter, M. Esselborn, M. Fiebig, B. Heese, P. Knippertz, D. Muller, A. Schladitz, and W. von Hoyningen-Huene, 2008. Desert dust aerosol air mass mapping in the western Sahara, using particle properties derived from space-based multi-angle imaging, *Tellus*, doi:10.1111/j.1600-0889.2008.00398.x.

Kahn, R.A., D.L. Nelson, M.Garay, R.C. Levy, M.A. Bull, J.V. Martonchik, D.J. Diner, S.R. Paradise, and E.G. Hansen, and L.A. Remer, 2009. MISR Aerosol product attributes, and statistical comparison with MODIS. *IEEE Trans. Geosci. Remt. Sens*, 4095-4114.

Kalashnikova, O.V., R. Kahn, I.N. Sokolik, and W-H. Li, 2005, The ability of multi-angle remote sensing observations to identify and distinguish mineral dust types: Part 1. Optical models and retrievals of optically thick plumes, *J. Geophys. Res. 110,*doi: 10.1029/2004JD004550.

Kalashnikova O. V., and R. Kahn 2006. Ability of multiangle remote sensing observations to identify and distinguish mineral dust types: Part 2. Sensitivity over dark water, J. Geophys. Res., 111, D11207, doi:10.1029/2005JD006756.

Kalashnikova, O.V., and R.A. Kahn, 2008. Mineral dust plume evolution over the Atlantic from combined MISR/MODIS aerosol retrievals, *J. Geophys. Res. 113*, D24204, doi:10.1029/2008JD010083.

Kim, D., and V. Ramanathan, 2008. Solar radiation budget and radiative forcing due to aerosol and clouds. *J. Geophys. Res.* 113, D02203, doi:10.1029/2007JD008434.

Kinne S., M. Schulz, C. Textor, et al., 2006. An AeroCom initial assessment -- optical properties in aerosol component modules of global models, *Atmos. Chem. Phys.* **6**:1815-1834.

1196 Kishcha, P., B. Starobinets, O. Kalashnikova, C. N. Long, and P. Alpert, 2009. Variations of
1197 meridional aerosol distribution and solar dimming. *J. Geophys. Res.,* 114,
1198 doi:10.1029/2008JD010975.
1199
1200 Levy, R.C., L.A. Remer, S. Mattoo, E.F. Vermote, and Y.J. Kaufman, 2007. Second-generation
1201 operational algorithm: Retrieval of aerosol properties over land from inversion of Moderate
1202 Resolution Imaging Spectroradiometer spectral reflectance, *J. Geophys. Res.*, 112,
1203 doi:10.1029/2006JD007811.
1204
1205 Levy, R.C., L.A. Remer, R.G. Kleidman, S. Mattoo, C. Ichoku, R. Kahn, and T.F. Eck, 2010.
1206 Global evaluation of the Collection 5 MODIS dark-target aerosol products over land. Atm.
1207 Chem. Phys. Discus, *submitted*.
1208
1209 Liu, Y., J.A. Sarnat, B.A. Coull, P. Koutrakis, and D.J. Jacob, 2004, Validation of MISR aerosol
1210 optical thickness measurements using Aerosol Robotic Network (AERONET) observations over
1211 the continuous United States, *J. Geophys. Res.*,109, doi:10.1029/2003JD003981.
1212
1213 Liu, Y., P. Koutrakis, and R. Kahn, 2007a. Estimating PM2.5 component concentrations and size
1214 distributions using satellite-retrieved fractional aerosol optical depth: Part 1 - Development of
1215 Methods, *J. Air & Waste Management Assoc.* 57, 1351-1359.
1216
1217 Liu, Y., P. Koutrakis, R. Kahn, S. Turquety, and R.M. Yantosca, 2007b. Estimating PM2.5
1218 component concentrations and size distributions using satellite-retrieved fractional aerosol
1219 optical depth: Part 2 - A case study, *J. Air & Waste Management Assoc*. 57, 1360-1369.
1220
1221 Martonchik, J.V., D.J. Diner, R. Kahn, M.M. Verstraete, B. Pinty, H.R. Gordon, and T.P.
1222 Ackerman, 1998. Techniques for the Retrieval of aerosol properties over land and ocean using
1223 multiangle imaging, IEEE Trans. Geosci. Remt. Sensing 36, 1212-1227.
1224
1225 Martonchik, J.V., D.J. Diner, K. Crean, and M. Bull, 2002. Regional aerosol retrieval results
1226 from MISR, IEEE Trans. Geosci. Remt. Sensing 40, 1520-1531.
1227

1228 Martonchik, J.V., D.J. Diner, R.A. Kahn, B.J. Gaitley, and B.N. Holben, 2004, Comparison of
1229 MISR and AERONET aerosol optical depths over desert sites, *Geophys. Res. Let., 31,*
1230 doi:10.1029/2004GL019807.
1231
1232 Martonchik, J.V., R.A. Kahn, and D.J. Diner, 2009. Retrieval of Aerosol Properties over Land
1233 Using MISR Observations. In: Kokhanovsky, A., ed., Satellite Aerosol Remote Sensing Over
1234 Land. Springer, Berlin.
1235
1236 Pierce, J.R., R.A. Kahn, M.R. Davis, and J.M. Comstock, 2010. Detecting thin cirrus in MISR
1237 aerosol retrievals. *J. Geophys. Res.*, 115, D08201, doi:10.1029/2009JD013019.
1238
1239 Press, W.H., S.A. Teukolsky, W.T. Vetterling, and B.P. Flannery, 2007. *Numerical Recipes*,
1240 Third Edition, Cambridge University Press, pp. 1235.
1241
1242 Ramanathan, V., P.J. Crutzen, J.T. Kiehl, and D. Rosenfeld, 2001. Aerosols, climate, and the
1243 hydrological cycle, *Science* 294, 2119-2124.
1244
1245 Redemann, J., B. Schmid, J.A. Eilers, R. Kahn, R.C. Levy, P.B. Russell, J.M. Livingston, P.V.
1246 Hobbs, W.L. Smith, Jr., and B.N. Holben, 2005, Suborbital measurements of spectral aerosol
1247 optical depth and its variability at sub-satellite-grid scales in support of CLAMS, 2001, *J.*
1248 *Atmosph. Sci.*, 62(4):993-1007, doi: 10.1175/JAS3387.1.
1249
1250 Reidmiller, D.R., P.V. Hobbs, and R. Kahn, 2006, Aerosol optical properties and particle size
1251 distributions on the east coast of the United States, derived from airborne in situ and remote
1252 sensing measurements, *J. Atmosph., Sci. 63*, 785–814.
1253
1254 Remer, L. A., Y.J. Kaufman, D. Tanre, S. Mattoo, D.A. Chu, J.V. Martins, R.-R. Li, C. Ichoku,
1255 R.C. Levy, R.G. Kleidman, T.F. Eck, E. Vermote, and B.N. Holben, 2005. The MODIS aerosol
1256 algorithm, products, and validation, *J. Atmos. Sci., 62*, 947–973.
1257
1258 Remer, L.A., R.G. Kleidman, R.C. Levy, Y.J. Kaufman, D. Tanre, S. Mattoo, J.V. Martins, C.
1259 Ichoku, I. Koren, H. Yu, and B.N. Holben, 2008. Global aerosol climatology from the MODIS
1260 satellite sensors. J. Geophys. Res. 113, doi:10.1029/2007JD009661.
1261

1262 Schladits, A., T. Muller, A. Massling, N. Kaaden, K. Kandler, and A. Wiedensohler, 2008. In
1263 situ measurements of optical properties at Tinfou (Morocco) during the Saharan mineral dust
1264 experiment, SAMUM 2006. *Tellus doi:10.1111/j.1600-0889.2008.00397.x*
1265
1266 Schmid B., J. Redemann, P. B. Russell, P. V. Hobbs, D. L. Hlavka, M. J. McGill, B. N. Holben,
1267 E. J. Welton, J. R. Campbell, O. Torres, R. A. Kahn, D. J. Diner, M. C. Helmlinger, D. A. Chu,
1268 C. Robles Gonzalez, and G. de Leeuw, 2003. Coordinated airborne, spaceborne, and ground-
1269 based measurements of massive, thick aerosol layers during the dry season in southern Africa, *J.*
1270 *Geophys. Res*, 108(D13), 8496, doi:10.1029/2002JD002297.
1271
1272 Schuster G. L., O. Dubovik, B. N. Holben, 2006. Angstrom exponent and bimodal aerosol size
1273 distributions, *J. Geophys. Res. 111*, D07207, doi:10.1029/2005JD006328.
1274
1275 Smirnov A., B.N.Holben, T.F.Eck, O.Dubovik, and I.Slutsker, 2000. Cloud screening and quality
1276 control algorithms for the AERONET database, Rem.Sens.Env. 73, 337-349.
1277
1278 Smirnov A., B.N. Holben, I. Slutsker, D.M. Giles, C.R. McClain, T.F. Eck, S.M. Sakerin, A.
1279 Macke, P. Croot, G. Zibordi, P.K. Quinn, J. Sciare, S. Kinne, M. Harvey, T.J. Smyth, S. Pikety,
1280 T. Zielinski, A. Proshutinsky, J.I. Goes, N.B. Nelson, P. Larouche, V.F. Radionov, P. Goloub. K.
1281 Krishnamoorthy, R. Matarrese, E.J. Robertson, and F. Jourdin, 2009. Maritime Aerosol Network
1282 as a component of Aerosol Robotic Network. *J. Geophys. Res. 114*, D06204,
1283 doi:10.1029/2008JD011257.
1284
1285 Van Donkelaar, A., R.V. Martin, M. Brauer, R. Kahn, R. Levy, C. Verduzco, and P. Villeneuve,
1286 2010. Global estimates of average ground-level fine particulate matter concentrations from
1287 satellite-based aerosol optical depth. *Environ. Health Perspect., in press.*
1288
1289 Yu, H., Y.J. Kaufman, M. Chin, G. Feingold, L.A. Remer, T.L. Anderson, Y. Balkanski, N.
1290 Bellouin, O. Boucher, S. Christopher, P. DeCola, R. Kahn, D. Koch, N. Loeb, M.S. Reddy, M.
1291 Schulz, T. Takemura, and M. Zhou, A Review of measurement-based assessment of aerosol
1292 direct radiative effect and forcing, *Atmosph. Chem. and Phys. 6*, 613-666, 2006.
1293

Zhang J., and S. Christopher, 2003. Longwave radiative forcing of Saharan dust aerosols estimated from MODIS, MISR, and CERES observations on Terra, *Geophys. Res. Lett.* **30**:2188, doi:10.1029/2003GL018479.

Zhao, G. and Di Girolamo, L., 2004. A Cloud Fraction versus View Angle Technique for Automatic In-Scene Evaluation of the MISR Cloud Mask, *Journal of Applied Meteorology*, **43** (6), 860-869.

Zhao, G., L. Di Girolamo, S. Dey, A. L. Jones, and M. Bull, 2009. Examination of direct cumulus contamination on MISR-retrieved aerosol optical depth and angstrom coefficient over ocean, *Geophys. Res. Lett. 36*, L13811, doi: 10.1029/2009GL038549.

Figure Captions

Figure 1. Geographical distribution of the 81 sites used in this study. Sites are color-coded according to expected aerosol air mass type: Biomass Burning – brown, Continental – green, Dusty – orange, Maritime – blue, Urban – gray, and Hybrid (smoke + dust) – red.

Figure 2. MISR-AERONET mean AOD difference (%) for 5,156 coincidences, stratified according to the aerosol air mass type class that frequently dominates the site. Comparisons between MISR central retrieval region AOD and near-coincident AERONET values are shown along the horizontal axis. The vertical axis gives the difference between MISR AOD, assessed as the average of the central plus all available of the eight surrounding regions, and the corresponding value assessed using the MISR central region only. Filled diamonds represent the class-average percent meeting the [0.05 or 20% × AOD] criterion. Filled circles plot the class-average percent meeting the more stringent [0.03 or 10% × AOD] criterion. Open symbols show corresponding class-average results for the MISR Version 12 product [from *Kahn et al.*, 2005]. Colors are used to distinguish aerosol type classes, as indicated in the legend. Lines connect the symbols for clarity. Numerical values for the central retrieval region statistics, along with the number of counts per site and per class and site-specific statistics, are given in Table 5. From the MISR-central statistics, 193 outliers were removed, but not from the central + surroundings statistics.

Figure 3. (Top row) Mid-visible (558 nm) MISR vs. AERONET coincident AOD scatter plots, stratified based on six broad aerosol type categories expected to dominate, at least during some seasons, at each site. Seasonality is represented by color: DJF – orange; MAM – blue; JJA – green; SON – orange. (Middle row) Magnified versions of the top-row scatter plots, for AOD between 0 and 0.2, which reduces over-plotting and helps clarify seasonality. (Bottom row) [MISR – AERONET] vs. AERONET difference plots for the full set of mid-visible coincident AOD data, stratified and color-coded as above. The AERONET data have been interpolated to the MISR effective wavelength for all cases. Statistics associated with these plots are given in Table 5.

Figure 4. Difference plot showing comparisons between MISR over-water algorithm mid-visible AOD retrieval results and near-coincident AERONET retrievals over Island sites (green open circles) and shipboard, hand-held sun photometer observations (blue open squares) from AERONET's Marine Aerosol Network (MAN) [*Smirnov et al.*, 2009]. Green and blue plus symbols indicate scenes dominated by broken cloud or dust plumes, and AERONET sites in relatively shallow, polluted waters of the Arabian Gulf (Abu Al Bukhoosh and Sir Bu Nuair) are identified with orange exes. AERONET AOD is used for the horizontal axis, blue lines mark zero-difference and bracket the 0.05 or 20% AOD envelope, and a red line marks the +0.025 MISR AOD offset discussed in Section 3.1.

Figure 5. MISR-MODIS outliers. Geographic distributions of coincident MISR and MODIS AOD retrieval cases where the ABS[MISR_AOD – MODIS_AOD] > 0.125 for the over-ocean plots, and > 0.2 for the over-land plots, color coded by region. (a) January 2006 over land; (b) July 2006 over land; (c) January 2006 over ocean; (d) July 2006 over ocean. The insets show difference plots of [MISR_AOD – MODIS_AOD] vs. MODIS AOD, color coded with the same scheme as the respective maps, but over-plotted, so some information is lost where the data overlap.

Figure 6. MISR-retrieved aerosol types. These histograms show the number of lowest-residual occurrences of each aerosol mixture, for all events within the MISR-AERONET coincident event data set having mid-visible MISR AOD > 0.15. The data are stratified by sites where each of the six broad aerosol air mass type categories are expected, at least in some seasons. Attempts at further stratification by aerosol air mass type proved unhelpful, due to site-to-site differences in seasonality, inter-annual variability, and limited event-by-event aerosol type information.

Mixture definitions are given in Table 3, and the histograms are color-coded to identify mixtures containing spherical, non-absorbing particles of various sizes, those that include spherical absorbing particles, and mixtures having non-spherical dust along with spherical components. The same color scheme is used in Figure 7. Note that the vertical scales vary from panel to panel, depending on available sample size.

Figure 7. Global map showing the distribution of retrieved Spherical Non-absorbing, Spherical Absorbing, and Non-spherical components, for the July 2007 MISR V22 aerosol product. In each $1^\circ \times 1^\circ$ bin, the lowest-residual mixtures are considered. The fraction AOD of all spherical non-absorbing components in the lowest-residual mixture is multiplied by the retrieved AOD for each observation, summed for the entire month, and assigned to the cyan color. The fractions of spherical absorbing and non-spherical components are processed similarly, and assigned to magenta and yellow, respectively. Linear, ternary mixing is used to assign the overall color to the $1^\circ \times 1^\circ$ bin, with pure cyan, magenta, and yellow as the three end-members. AOD-weighting de-emphasizes the low-AOD retrievals for which the retrieved particle properties are less certain. The retrieved aerosol properties reflect many of the expected regional-scale patterns as well as some artifacts, as discussed in the text.

Figure 8. [MISR-AERONET] ANG vs. AERONET AOD is shown in rows 1 through 3 for locations dominated, at least during some seasons, by: Biomass Burning (a-d), Dusty (f-i), and Continental (k-n) aerosol air mass types. The columns are distinguished by season. Column 5 provides the annual aggregate of [MISR-AERONET] ANG vs. AERONET ANG for the respective categories. Smaller dots are for cases where the AERONET AOD <0.15. The zero-difference lines are indicated by dashed horizontal lines, and dashed vertical lines mark AERONET AOD = 0.15 in the panels of the first four columns. For plots in the fifth column, the MISR ANG=1 line is drawn.

Figure 9. Angstrom Exponent (ANG) Cluster Analysis. Row 1 presents the MISR vs. AERONET ANG scatter plots, partitioned into K-means clusters, with K=3, for each of the six aerosol air mass type categories. Initial cluster seeds are shown as open circles, and final cluster centers are indicated as solid black dots; the quantitative cluster centroid locations are given in the annotation of each plot. Row 2 shows the corresponding MISR vs. AERONET AOD scatter plots, colored according to cluster. Seasonal information is encoded in the symbol shapes: DJF,

diamonds; MAM, triangles; JJA, squares; SON, circles. Rows 3-5 provide histograms of mixture number (Table 3) for all successful mixtures, similar in format to those Figure 6, but partitioned and color-coded according to cluster, for the ANG clusters identified with smaller (orange), intermediate (purple), and larger (green) column-effective particle sizes, respectively. Only cases having MISR AOD > 0.15 are included in this analysis, due to limited MISR aerosol property sensitivity for lower AOD, as illustrated in Figure 8; this accounts for the horizontal low-end cutoff in the AOD plots in Row 2. Note that the vertical scales in the Row 3-5 plots vary, based on the numbers of counts in each cluster.

Table 1. AERONET validation site locations, seasonal coverage, and MISR coincidence counts

Site Name	Lat	Long	Altitude (meters)	DJF	MAM	JJA	SON	Total Obs	Total Seasons
Biomass Burning									
Abracos_Hill	-10.76	-62.36	200	1	3	17	11	32	14
Alta_Floresta	-9.92	-56.02	175	0	4	20	9	33	18
Bonanza_Creek	64.74	-148.32	150	0	15	3	8	26	11
Cuiaba-Miranda	-15.73	-56.02	210	2	8	21	6	37	13
Jabiru	-12.66	132.89	30	6	11	42	27	86	18
Mongu	-15.25	23.15	1107	11	53	63	39	166	30
Mukdahan	16.61	104.68	166	31	14	1	8	54	14
Rio_Branco	-9.96	-67.87	212	1	1	7	7	16	9
SANTA_CRUZ	-17.80	-63.18	442	6	2	9	2	19	8
Skukuza	-24.99	31.59	150	9	35	50	30	124	30
Tinga_Tingana	-28.98	139.99	38	24	13	15	17	69	19
Continental									
Arica	-18.47	-70.31	25	20	14	2	9	45	15
Bondville	40.05	-88.37	212	18	19	12	27	76	26
BSRN_BAO_Boulder	40.04	-105.01	1604	10	17	53	28	108	27
Bratts_Lake	50.28	-104.70	586	0	12	35	19	66	18
COVE	36.90	-75.71	37	8	21	20	25	74	28
Cart_Site	36.61	-97.49	318	13	19	24	21	77	22
Cordoba-CETT	-31.52	-64.46	730	14	24	28	29	95	21
El_Arenosillo	37.10	-6.73	0	6	5	22	6	39	18
Forth_Crete	35.33	25.28	20	0	5	4	0	9	6

Konza_EDC	39.10	-96.61	341	24	16	41	26	107	26
Maricopa	33.07	-111.97	360	17	30	31	22	100	23
Nes_Ziona	31.92	34.79	40	9	18	32	16	75	23
Pimai	15.18	102.56	220	24	14	3	2	43	12
Rimrock	46.49	-116.99	824	8	10	36	21	75	23
Rogers_Dry_Lake	34.93	-117.89	680	20	53	63	31	167	20
Sevilleta	34.35	-106.89	1477	8	22	39	11	80	24
Sioux_Falls	43.74	-96.63	500	4	11	30	25	70	20
Toravere	58.26	26.46	70	0	16	12	14	42	16
Dusty									
Anmyon	36.54	126.33	47	2	9	5	4	20	13
Birdsville	-25.90	139.35	46	12	4	3	7	26	7
Capo_Verde	16.73	-22.93	60	18	21	18	14	71	27
Dakar	14.39	-16.96	0	20	17	14	20	71	19
Dalanzadgad	43.58	104.42	1470	30	28	15	34	107	27
Dhadnah	25.51	56.33	81	2	13	16	7	38	13
Hamim	22.97	54.30	209	5	15	6	13	39	13
Mezaira	23.15	53.78	204	0	0	9	3	12	3
Mussafa	24.37	54.47	10	6	7	7	10	30	7
Railroad_Valley	38.50	-115.96	1435	16	14	44	47	121	18
Solar_Village	24.91	46.41	650	7	33	59	11	110	25
Maritime									
Ascension_Island	-7.98	-14.41	30	16	5	14	8	43	19
Azores	38.53	-28.63	50	0	2	6	2	10	8
Bermuda	32.37	-64.70	10	0	2	5	3	10	8
La_Jolla	32.87	-117.25	115	10	18	17	11	56	19

Lanai	20.74	-156.92	20	13	16	12	7	48	14
Midway_Island	28.21	-177.38	0	15	7	16	12	50	14
Nauru	-0.52	166.92	7	1	7	1	10	19	10
Rottnest_Island	-32.00	115.30	40	16	17	7	6	46	10
San_Nicolas	33.26	-119.49	133	6	11	5	7	29	16
Tahiti	-17.58	-149.61	98	2	7	9	7	25	13
UCSB	34.42	-119.85	33	11	8	7	16	42	12
Urban									
Avignon	43.93	4.88	32	34	44	65	41	184	30
Bac_Giang	21.29	106.23	15	4	3	1	10	18	9
Beijing	39.98	116.38	92	25	33	25	32	115	24
Belsk	51.84	20.79	190	0	7	10	7	24	14
CCNY	40.82	-73.95	100	11	12	10	18	51	21
Fresno	36.78	-119.77	110	10	24	46	37	117	23
GSFC	38.99	-76.84	87	31	38	7	40	116	29
Hamburg	53.57	9.97	105	6	20	12	22	60	19
Ispra	45.80	8.63	235	1	17	17	10	45	22
Kanpur	26.45	80.35	142	23	33	10	31	97	25
Lille	50.61	3.14	60	5	12	13	9	39	21
MD_Science_Center	39.28	-76.72	15	11	30	14	35	90	29
Mexico_City	19.33	-99.18	2268	20	26	5	5	56	19
Minsk	53.00	27.50	200	0	6	3	10	19	11
Moscow_MSU_MO	55.70	37.51	192	0	21	9	17	47	17
Osaka	34.65	135.59	50	5	11	1	4	21	17
Rome_Tor_Vergata	41.84	12.65	130	28	25	49	40	142	25
Sao_Paulo	-23.56	-46.74	865	9	11	24	24	68	24

Shirahama	33.69	135.36	10	3	5	5	0	13	11
Thessaloniki	40.63	22.96	60	6	9	9	8	32	10
Tomsk	56.48	85.05	130	0	7	12	13	32	15
XiangHe	39.75	116.96	36	23	21	12	31	87	15
Yulin	38.28	109.72	1080	0	9	7	9	25	6
Hybrid_BD									
Banizoumbou	13.54	2.66	250	50	29	20	45	144	28
DMN_Maine_Sorokok	13.22	12.02	350	19	10	4	9	42	9
Djougou	9.76	1.60	400	14	9	1	7	31	12
IER_Cinzana	13.28	-5.93	285	39	27	18	33	117	15
Ilorin	8.32	4.34	350	20	11	0	5	36	15
Ouagadougou	12.20	-1.40	290	20	11	0	17	67	21
Sede_Boker	30.85	34.78	480	22	48	62	56	188	32

Table 2. MISR Version 22 Aerosol Component Optical Models*

#	Component Name	r_1 (μm)	r_2 (μm)	r_c (μm)	σ	SSA (446)	SSA (558)	SSA (672)	SSA (866)	AOD(446)/ AOD(558)	AOD(672)/ AOD(558)	AOD(867)/ AOD(558)	g (558)	Particle Size/Shape Category
1	**sph_nonabsorb_0 .06**	0.001	0.4	0.03	1.65	1.00	1.00	1.00	1.00	1.95	0.55	0.23	0.352	Small Spherical
2	**sph_nonabsorb_0 .12**	0.001	0.75	0.06	1.7	1.00	1.00	1.00	1.00	1.54	0.66	0.35	0.609	Small Spherical
3	**sph_nonabsorb_0 .26**	0.01	1.5	0.12	1.75	1.00	1.00	1.00	1.00	1.18	0.82	0.58	0.717	Medium Spherical
6	**sph_nonabsorb_2 .80**	0.10	50.	1.0	1.9	1.00	1.00	1.00	1.00	0.99	1.02	1.06	0.776	Large Spherical
8	**sph_absorb_0.12_ ssa_green_0.9**	0.001	0.75	0.06	1.7	0.91	0.90	0.89	0.85	1.50	0.68	0.37	0.612	Small Spherical moderately absorbing
14	**sph_absorb_0.12_ ssa_green_0.8**	0.001	0.75	0.06	1.7	0.82	0.80	0.77	0.72	1.47	0.69	0.40	0.614	Small Spherical strongly absorbing
19	**Medium_grains**	0.10	1.00	0.5	1.5	0.92	0.98	0.99	1.00	0.90	1.06	1.08	0.711	Medium Dust
21	**Coarse_spheroids**	0.10	6.0	1.0	2.0	0.81	0.90	0.97	0.98	0.99	1.02	1.05	0.772	Coarse Dust

*These aerosol optical models apply to the MISR standard Level 2AS aerosol product, Versions 16 through 22. A number-weighted, log-normal particle size distribution function is adopted for all components. Aerosol components are named based on particle shape (spherical, non-spherical grains or spheroids), SSA (non-absorbing or absorbing) and effective radius (in μm). For absorbing aerosols, the green-band SSA is also given. Single scattering properties were calculated using a Mie code for the spherical particles; the dust component properties were calculated using the Discrete Dipole and T-matrix approaches for medium and coarse modes, respectively [Kalashnikova et al., 2005]. Wavelength in nm is specified in parentheses where

appropriate. r_1 and r_2 are the upper and lower limits of the size distribution, r_c and □ are the characteristic radius and width parameters in the log-normal distribution, and SSA is the single-scattering albedo. The asymmetry parameter (g) will generally represent particle scattering phase functions poorly for the purpose of calculating MISR multi-angle radiances, and is given here only in MISR green band for reference; full phase functions are available in the MISR standard product "ACP_APOP" files. All spherical components are assumed to be distributed vertically within 10 km of the surface, and have scale heights of 2 km. Medium dust is confined to the lowest 10 km, and coarse dust is confined to the lowest 10 km.

Table 3. MISR Version 22 Aerosol Mixture Properties[§]

Mixture	Component Fractional AOD (at 558 nm)								AOD rel. to green			Single Scattering Albedo				ANG
#	1*	2*	3*	6*	8*	14*	19*	21*	blue	red	nir	blue	green	red	nir	
Spherical, Non-absorbing Mixtures																
1	1	-	-	-	-	-	-	-	1.95	0.549	0.23	1	1	1	1	**3.23**
2	0.95	-	-	0.05	-	-	-	-	1.9	0.573	0.271	1	1	1	1	2.94
3	0.9	-	-	0.1	-	-	-	-	1.85	0.596	0.312	1	1	1	1	2.69
4	0.8	-	-	0.2	-	-	-	-	1.76	0.644	0.395	1	1	1	1	2.26
5	0.7	-	-	0.3	-	-	-	-	1.66	0.691	0.477	1	1	1	1	1.88
6	0.6	-	-	0.4	-	-	-	-	1.57	0.738	0.559	1	1	1	1	1.55
7	0.5	-	-	0.5	-	-	-	-	1.47	0.786	0.642	1	1	1	1	1.24
8	0.4	-	-	0.6	-	-	-	-	1.37	0.833	0.724	1	1	1	1	0.96
9	0.3	-	-	0.7	-	-	-	-	1.28	0.881	0.807	1	1	1	1	0.69
10	0.2	-	-	0.8	-	-	-	-	1.18	0.928	0.889	1	1	1	1	0.42
11	-	1	-	-	-	-	-	-	1.54	0.66	0.348	1	1	1	1	2.24
12	-	0.95	-	0.05	-	-	-	-	1.51	0.679	0.384	1	1	1	1	2.07
13	-	0.9	-	0.1	-	-	-	-	1.49	0.697	0.419	1	1	1	1	1.91
14	-	0.8	-	0.2	-	-	-	-	1.43	0.733	0.49	1	1	1	1	1.62
15	-	0.7	-	0.3	-	-	-	-	1.38	0.769	0.56	1	1	1	1	1.36
16	-	0.6	-	0.4	-	-	-	-	1.32	0.805	0.631	1	1	1	1	1.11
17	-	0.5	-	0.5	-	-	-	-	1.26	0.842	0.701	1	1	1	1	0.89
18	-	0.4	-	0.6	-	-	-	-	1.21	0.878	0.772	1	1	1	1	0.68
19	-	0.3	-	0.7	-	-	-	-	1.15	0.914	0.843	1	1	1	1	0.47
20	-	0.2	-	0.8	-	-	-	-	1.1	0.95	0.913	1	1	1	1	0.28
21	-	-	1	-	-	-	-	-	1.18	0.82	0.576	1	1	1	1	1.09
22	-	-	0.95	0.05	-	-	-	-	1.17	0.83	0.6	1	1	1	1	1.02
23	-	-	0.9	0.1	-	-	-	-	1.17	0.841	0.624	1	1	1	1	0.94

24	-	-	0.8	0.2	-	-	-	-	1.15	0.861	0.672	1	1	1	1	0.81
25	-	-	0.7	0.3	-	-	-	-	1.13	0.881	0.72	1	1	1	1	0.68
26	-	-	0.6	0.4	-	-	-	-	1.11	0.901	0.767	1	1	1	1	0.55
27	-	-	0.5	0.5	-	-	-	-	1.09	0.921	0.815	1	1	1	1	0.43
28	-	-	0.4	0.6	-	-	-	-	1.07	0.942	0.863	1	1	1	1	0.32
29	-	-	0.3	0.7	-	-	-	-	1.05	0.962	0.911	1	1	1	1	0.21
30	-	-	0.2	0.8	-	-	-	-	1.03	0.982	0.959	1	1	1	1	0.10
Spherical, Absorbing + Non-absorbing Mixtures																
31	-	-	-	-	1	-	-	-	1.51	0.677	0.375	0.911	0.9	0.885	0.8	2.10
32	-	-	-	0.05	0.95	-	-	-	1.48	0.694	0.409	0.914	0.905	0.894	0.8	1.96
33	-	-	-	0.1	0.9	-	-	-	1.45	0.712	0.443	0.917	0.91	0.902	0.8	1.80
34	-	-	-	0.2	0.8	-	-	-	1.4	0.746	0.511	0.924	0.92	0.917	0.9	1.53
35	-	-	-	0.3	0.7	-	-	-	1.35	0.781	0.578	0.931	0.93	0.93	0.9	1.28
36	-	-	-	0.4	0.6	-	-	-	1.3	0.815	0.646	0.938	0.94	0.943	0.9	1.05
37	-	-	-	0.5	0.5	-	-	-	1.25	0.85	0.714	0.946	0.95	0.954	0.9	0.84
38	-	-	-	0.6	0.4	-	-	-	1.2	0.884	0.782	0.955	0.96	0.965	0.9	0.64
39	-	-	-	0.7	0.3	-	-	-	1.14	0.919	0.85	0.965	0.97	0.975	0.9	0.44
40	-	-	-	0.8	0.2	-	-	-	1.09	0.953	0.918	0.976	0.98	0.984	0.9	0.26
41	-	-	-	-	-	1	-	-	1.47	0.695	0.403	0.821	0.8	0.773	0.7	1.95
42	-	-	-	0.05	-	0.95	-	-	1.45	0.712	0.436	0.827	0.81	0.79	0.7	1.81
43	-	-	-	0.1	-	0.9	-	-	1.42	0.728	0.468	0.833	0.82	0.805	0.7	1.68
44	-	-	-	0.2	-	0.8	-	-	1.37	0.761	0.533	0.847	0.84	0.834	0.8	1.43
45	-	-	-	0.3	-	0.7	-	-	1.33	0.793	0.598	0.861	0.86	0.861	0.8	1.20
46	-	-	-	0.4	-	0.6	-	-	1.28	0.826	0.664	0.876	0.88	0.886	0.8	0.99
47	-	-	-	0.5	-	0.5	-	-	1.23	0.859	0.729	0.893	0.9	0.908	0.9	0.79
48	-	-	-	0.6	-	0.4	-	-	1.18	0.892	0.794	0.911	0.92	0.929	0.9	0.60
49	-	-	-	0.7	-	0.3	-	-	1.13	0.924	0.859	0.93	0.94	0.949	0.9	0.42
50	-	-	-	0.8	-	0.2	-	-	1.08	0.957	0.924	0.952	0.96	0.967	0.9	0.24
Dust Mixtures																

51	-	0.72	-	0.08	-	-	0.2	-	1.37	0.77	0.551	0.989	0.995	0.998	0.9	1.37
52	-	0.48	-	0.32	-	-	0.2	-	1.24	0.857	0.72	0.988	0.995	0.999	0.9	0.81
53	-	0.16	-	0.64	-	-	0.2	-	1.06	0.973	0.946	0.986	0.995	0.999	0.9	0.17
54	-	0.54	-	0.06	-	-	0.4	-	1.25	0.844	0.683	0.977	0.991	0.997	0.9	0.91
55	-	0.36	-	0.24	-	-	0.4	-	1.15	0.909	0.81	0.975	0.991	0.997	0.9	0.53
56	-	0.12	-	0.48	-	-	0.4	-	1.02	0.996	0.979	0.972	0.991	0.998	0.9	0.05
57	-	0.36	-	0.04	-	-	0.6	-	1.13	0.918	0.815	0.962	0.986	0.996	0.9	0.49
58	-	0.24	-	0.16	-	-	0.6	-	1.07	0.961	0.9	0.959	0.986	0.996	0.9	0.25
59	-	0.08	-	0.32	-	-	0.6	-	0.977	1.02	1.01	0.956	0.986	0.997	0.9	-0.06
60	-	0.18	-	0.02	-	-	0.8	-	1.01	0.991	0.947	0.943	0.982	0.995	0.9	0.10
61	-	0.12	-	0.08	-	-	0.8	-	0.98	1.01	0.989	0.941	0.982	0.995	0.9	-0.02
62	-	0.04	-	0.16	-	-	0.8	-	0.936	1.04	1.05	0.938	0.982	0.995	0.9	-0.17
63	-	0.4	-	-	-	-	0.48	0.12	1.16	0.898	0.783	0.951	0.977	0.993	0.9	0.60
64	-	0.4	-	-	-	-	0.36	0.24	1.18	0.892	0.78	0.94	0.968	0.99	0.9	0.62
65	-	0.4	-	-	-	-	0.24	0.36	1.19	0.887	0.776	0.928	0.959	0.986	0.9	0.64
66	-	0.4	-	-	-	-	0.12	0.48	1.2	0.881	0.773	0.918	0.95	0.983	0.9	0.66
67	-	0.2	-	-	-	-	0.64	0.16	1.04	0.977	0.928	0.927	0.97	0.991	0.9	0.17
68	-	0.2	-	-	-	-	0.48	0.32	1.05	0.969	0.924	0.91	0.958	0.987	0.9	0.20
69	-	0.2	-	-	-	-	0.32	0.48	1.07	0.962	0.919	0.894	0.946	0.983	0.9	0.23
70	-	0.2	-	-	-	-	0.16	0.64	1.08	0.954	0.914	0.879	0.934	0.979	0.9	0.25
71	-	-	-	-	-	-	0.8	0.2	0.914	1.06	1.07	0.896	0.962	0.99	0.9	-0.24
72	-	-	-	-	-	-	0.6	0.4	0.933	1.05	1.07	0.873	0.947	0.985	0.9	-0.20
73	-	-	-	-	-	-	0.4	0.6	0.951	1.04	1.06	0.851	0.932	0.98	0.9	-0.17
74	-	-	-	-	-	-	0.2	0.8	0.97	1.03	1.06	0.83	0.917	0.976	0.9	-0.13

[§] The eight components used in this mixture table are described in Table 2.

Table 4. AOD and Sky-scan Coincidence Sampling, by Season and Aerosol Type

	Total	DJF	MAM	JJA	SON
BiomassBurning					
Central AOD	662	91	159	248	164
Surrounding AOD	653	89	157	244	163
Central Sky scan	318	39	75	110	94
Lowest Residual nonabsorbing	383	57	99	139	88
Lowest Residual absorbing	199	17	43	90	49
Lowest Residual dusty	80	17	17	19	27
Continental					
Central AOD	1348	202	326	488	332
Surrounding AOD	1342	200	325	486	331
Central Sky scan	496	90	134	130	130
Lowest Residual nonabsorbing	990	158	218	357	257
Lowest Residual absorbing	178	22	44	71	41
Lowest Residual dusty	180	22	64	60	34
Dusty					
Central AOD	645	118	161	196	170
Surrounding AOD	641	117	159	196	169
Central Sky scan	300	41	81	101	77
Lowest Residual nonabsorbing	299	67	63	72	97
Lowest Residual absorbing	120	30	26	22	42
Lowest Residual dusty	226	21	72	102	31
Maritime					
Central AOD	378	90	100	99	89
Surrounding AOD	378	90	100	99	89
Central Sky scan	81	20	27	19	15
Lowest Residual nonabsorbing	157	41	36	48	32
Lowest Residual absorbing	61	11	10	23	17
Lowest Residual dusty	160	38	54	43	59
Urban					
Central AOD	1498	255	424	366	453
Surrounding AOD	1480	249	420	363	448
Central Sky scan	648	122	180	103	243
Lowest Residual nonabsorbing	1027	170	269	275	313

Lowest Residual absorbing	242	49	64	48	81
Lowest Residual dusty	229	36	91	43	59
	Hybrid_BD				
Central AOD	625	188	155	110	172
Surrounding AOD	620	187	153	109	171
Central Sky scan	287	98	70	36	83
Lowest Residual nonabsorbing	227	63	33	42	89
Lowest Residual absorbing	131	33	32	29	37
Lowest Residual dusty	267	92	90	39	46

Nonabsorbing mixtures are 1-30, absorbing mixtures are 31-50, and dusty mixtures are 51-74 in Table 3.

Table 5. MISR-AERONET Green-band AOD Comparison Statistics for central regions without outliers and for surroundings, stratified by Site and by Expected Aerosol Type Category[†]

Site	Count	MISR AOD		AERONET AOD		AOD Corr	Mean Abs Diff (Rel) %	AOD Gain	AOD Offset	AOD: 20% or 0.05	AOD: 10% or 0.03	DAOD: Surr - Cntr	V12 AOD: 20% or 0.05/ 10% or 0.03
		Mean	Stdv	Mean	Stdv								
BiomassBurning	***635***	***0.191***	***0.024***	***0.215***	***0.013***	***0.930***	***32.49***	***0.653***	***0.050***	***76.38***	***54.96***	***2.0 / 1.7***	***66/39***
Abracos_Hill	31	0.242	0.018	0.300	0.017	0.960	19.72	0.700	0.032	74.19	54.84	0.8 / -1.7	
Mukdahan	54	0.332	0.027	0.396	0.022	0.922	19.97	0.740	0.039	62.96	46.30	-5.6 / -9.3	
Mongu	165	0.213	0.025	0.217	0.011	0.955	22.39	0.837	0.031	87.27	69.09	2.5 / 3.8	
Skukuza	123	0.141	0.019	0.154	0.008	0.950	23.81	0.834	0.013	86.99	66.67	2.5 / 1.1	
Jabiru	85	0.103	0.023	0.109	0.009	0.902	26.99	0.838	0.011	87.06	67.06	3.6 / 7.4	
Rio_Branco	16	0.321	0.031	0.501	0.024	0.966	30.66	0.470	0.085	37.50	25.00	12.5 / -6.3	
Alta_Floresta	32	0.310	0.028	0.443	0.036	0.918	31.31	0.530	0.075	59.38	37.50	10.3 / 1.9	
Cuiaba-Miranda	33	0.246	0.028	0.349	0.024	0.984	31.96	0.688	0.006	57.58	18.18	-6.2 / 8.8	
Santa_Cruz	19	0.158	0.025	0.161	0.011	0.905	36.11	0.481	0.081	68.42	42.11	21.1 / 10.5	
Bonanza_Creek	26	0.071	0.007	0.057	0.005	0.726	55.77	0.802	0.025	80.77	65.39	3.8 / 7.7	
Tinga_Tingana	51	0.130	0.033	0.074	0.008	0.837	104.67	1.064	0.050	49.02	13.73	4.6 / 6.6	
Dusty	***585***	***0.283***	***0.039***	***0.270***	***0.015***	***0.874***	***50.83***	***0.766***	***0.077***	***49.57***	***28.21***	***5.0 / 0.9***	***55/37***
Mezaira	12	0.392	0.077	0.352	0.011	0.658	21.11	0.901	0.075	83.33	50.00	0.0 / 16.7	

Capo_Verde	71	0.356	0.032	0.367	0.018	0.849	22.30	0.872	0.037	54.93	29.58	7.0 / 1.55	
Dhadnah	37	0.377	0.049	0.404	0.020	0.785	23.37	0.946	-0.005	43.24	35.14	9.4 / -6.2	
Solar_Village	108	0.378	0.062	0.341	0.019	0.915	26.03	0.735	0.127	58.33	37.04	-1.1 / -8.9	
Anmyon	19	0.389	0.026	0.524	0.035	0.950	26.39	0.723	0.010	36.84	26.32	-11.8 /-11.3	
Mussafa	30	0.343	0.046	0.303	0.018	0.815	29.55	1.072	0.018	50.00	33.33	30.0 / 13.3	
Dakar	70	0.332	0.034	0.440	0.020	0.861	30.11	0.719	0.016	32.86	14.29	10.8 / 2.6	
Hamim	39	0.380	0.056	0.286	0.014	0.888	37.49	1.291	0.011	33.33	23.08	-5.1 /-7.7	
Dalanzadgad	86	0.139	0.018	0.090	0.009	0.825	78.64	0.928	0.055	59.30	31.40	-5.1 / -0.6	
Railroad_Valley	99	0.117	0.025	0.064	0.005	0.722	107.56	1.143	0.044	50.51	24.24	17.3 / 6.3	
Birdsville	14	0.123	0.035	0.057	0.005	0.889	132.49	1.421	0.041	21.43	0.00	-6.0 / 3.8	
Continental	***1294***	***0.142***	***0.030***	***0.128***	***0.010***	***0.859***	***49.00***	***0.721***	***0.050***	***69.78***	***49.38***	***3.0 / 0.5***	***63/42***
Pimai	43	0.314	0.035	0.357	0.022	0.810	20.07	0.615	0.095	62.79	41.86	18.6 / 11.6	
Nes_Ziona	75	0.230	0.047	0.273	0.023	0.916	21.56	0.799	0.012	64.00	34.67	8.0 / 13.3	
Toravere	40	0.124	0.012	0.123	0.009	0.944	22.05	0.917	0.011	92.50	77.50	-2.0 / 5.8	
Arica	43	0.201	0.039	0.264	0.016	0.685	29.91	0.698	0.017	44.19	23.26	26.9 / 19.0	
El_Arenosillo	36	0.160	0.033	0.208	0.011	0.867	30.51	0.714	0.012	44.44	27.78	37.6 / 26.1	
Konza_EDC	106	0.114	0.021	0.109	0.008	0.854	30.84	0.686	0.039	86.79	72.64	2.9 / 4.9	
Cordoba-CETT	93	0.064	0.012	0.075	0.008	0.907	32.28	0.621	0.017	93.55	82.80	0.1 / 0.4	
Cart_Site	76	0.125	0.026	0.105	0.007	0.895	36.69	0.874	0.033	84.21	64.47	2.8 / -2.1	
Bondville	76	0.123	0.021	0.123	0.009	0.890	38.00	0.635	0.045	82.90	59.21	-3.9 /-10.5	

Forth_Crete	8	0.202	0.018	0.314	0.014	0.908	38.59	1.234	-0.186	37.50	0.00	18.1 / 11.1	
Sioux_Falls	69	0.112	0.018	0.096	0.007	0.888	39.47	1.059	0.010	81.16	68.12	1.7 / -1.0	
Rimrock	72	0.106	0.021	0.081	0.006	0.823	50.94	0.999	0.025	77.78	50.00	16.9 / 26.0	
Boulder	105	0.121	0.034	0.092	0.008	0.838	53.23	0.906	0.038	72.38	57.14	-2.0 /-7.1	
COVE	74	0.213	0.028	0.175	0.016	0.979	53.45	0.934	0.049	68.92	33.78	-4.1 / 0.0	
Maricopa	99	0.128	0.038	0.091	0.007	0.699	55.72	0.940	0.043	68.69	48.49	2.3 / -4.5	
Bratts_Lake	64	0.127	0.023	0.107	0.011	0.800	56.31	0.507	0.073	78.13	59.38	-3.9 /-9.4	
Sevilleta	70	0.159	0.049	0.095	0.006	0.927	90.88	1.004	0.064	32.86	20.00	4.6 / 2.5	
Rogers_Dry_Lake	145	0.135	0.045	0.074	0.005	0.715	96.43	1.343	0.036	46.21	19.31	-4.3 /-11.5	
Urban	***1467***	***0.203***	***0.028***	***0.237***	***0.021***	***0.924***	***26.90***	***0.662***	***0.046***	***70.76***	***49.42***	***-4.5 /-1.2***	
Belsk	23	0.182	0.020	0.197	0.020	0.964	14.22	0.938	-0.003	82.61	60.87	9.1 / 10.0	
Moscow	47	0.166	0.016	0.181	0.017	0.907	18.90	0.746	0.032	87.23	57.45	-4.3 / 10.6	
Mexico_City	56	0.243	0.031	0.273	0.043	0.918	20.02	0.748	0.039	71.43	44.64	-32.1 /-21.4	
Bac_Giang	18	0.545	0.045	0.655	0.030	0.803	21.03	0.488	0.225	61.11	33.33	-16.7 /-11.1	
Tomsk	31	0.168	0.021	0.196	0.017	0.973	21.16	0.779	0.016	80.65	61.29	-2.5 / 7.5	
MD_Science_Center	89	0.140	0.017	0.150	0.016	0.957	22.51	0.773	0.023	87.64	70.79	1.2 / 5.9	
Hamburg	60	0.159	0.017	0.160	0.017	0.921	22.81	0.961	0.005	85.00	65.00	0.0 / 3.3	
Shirahama	13	0.286	0.024	0.372	0.020	0.933	22.91	0.716	0.020	46.15	23.08	7.7 / 23.1	
Rome_Tor_Vergata	141	0.144	0.025	0.165	0.017	0.869	23.05	0.795	0.012	74.47	53.19	-7.6 /-10.9	
Lille	39	0.155	0.021	0.186	0.017	0.935	23.77	0.736	0.018	71.80	51.28	5.1 / 5.1	

Beijing	113	0.292	0.041	0.381	0.033	0.930	24.21	0.620	0.056	54.87	38.94	1.7 / -4.2	
Sao_Paulo	66	0.171	0.021	0.204	0.022	0.888	25.36	0.554	0.059	66.67	40.91	-2.0 / 3.2	
XiangHe	86	0.311	0.038	0.399	0.038	0.913	25.78	0.594	0.074	59.30	39.54	-1.8 / 1.8	
Kanpur	96	0.430	0.046	0.574	0.033	0.820	26.08	0.620	0.074	39.58	13.54	-6.6 / 1.9	
Thessaloniki	29	0.188	0.027	0.251	0.020	0.927	26.38	0.783	-0.008	48.28	31.03	-1.4 / 9.6	
Osaka	21	0.284	0.035	0.297	0.030	0.900	29.07	0.651	0.090	47.62	23.81	9.5 / 14.3	
Yulin	24	0.288	0.058	0.318	0.030	0.739	29.80	0.498	0.130	54.17	33.33	1.8 / -1.3	
GSFC	116	0.109	0.012	0.111	0.009	0.948	30.99	0.678	0.034	93.10	82.76	2.6 / -1.7	
Avignon	182	0.149	0.026	0.145	0.014	0.843	32.83	0.729	0.044	77.47	54.95	-3.6 /-2.8	
Ispra	31	0.178	0.023	0.256	0.024	0.869	33.46	0.689	0.002	41.94	12.90	-1.9 / 13.8	
Fresno	116	0.146	0.040	0.138	0.010	0.746	33.85	0.597	0.063	78.45	52.59	-21.2 /-13.3	
Minsk	19	0.175	0.018	0.167	0.013	0.930	35.46	1.064	-0.002	68.42	52.63	10.5 /-5.3	
CCNY	51	0.168	0.025	0.184	0.014	0.914	35.62	0.727	0.034	70.59	45.10	-2.0 / 11.8	
Maritime	***366***	***0.117***	***0.018***	***0.095***	***0.008***	***0.870***	***53.69***	***0.801***	***0.041***	***74.86***	***50.00***	***7.7 / 4.8***	***69/45***
Ascension_Island	43	0.193	0.035	0.195	0.010	0.944	28.27	0.768	0.043	76.74	48.84	0.0 / 0.0	
Nauru	19	0.087	0.008	0.070	0.007	0.776	31.86	0.976	0.018	89.47	68.42	0.0 / 10.5	
Bermuda	10	0.123	0.016	0.116	0.008	0.572	39.66	0.320	0.086	60.00	60.00	30.0 / 0.0	
Midway_Island	50	0.108	0.013	0.079	0.007	0.935	40.86	1.160	0.016	88.00	60.00	6.0 / 8.0	
Tahiti	25	0.071	0.014	0.067	0.010	0.518	42.93	0.456	0.041	92.00	72.00	0.0 / 4.0	
Azores	9	0.100	0.016	0.084	0.009	0.762	49.25	0.493	0.059	88.89	55.56	1.1 / 14.4	

La_Jolla	50	0.128	0.023	0.112	0.015	0.670	54.86	0.774	0.042	52.00	32.00	28.4 / 16.2	
Lanai	46	0.105	0.014	0.073	0.007	0.621	55.59	0.699	0.053	80.44	47.83	2.9 / 2.2	
Rottnest_Island	46	0.069	0.012	0.053	0.004	0.226	61.42	0.195	0.059	89.13	71.74	2.2 / -2.2	
UCSB	39	0.148	0.022	0.108	0.009	0.930	67.60	0.990	0.041	61.54	30.77	14.7 / 7.3	
San_Nicolas	29	0.115	0.018	0.067	0.004	0.755	107.30	0.839	0.059	51.72	24.14	0.0 / -3.4	
Hybrid_BD	***614***	***0.346***	***0.053***	***0.372***	***0.019***	***0.876***	***36.80***	***0.597***	***0.124***	***47.56***	***27.85***	***-2.3 /-0.7***	
Ouagadougou	66	0.347	0.041	0.427	0.021	0.907	20.84	0.553	0.111	59.09	33.33	-5.4 /-2.0	
Banizoumbou	142	0.425	0.066	0.460	0.023	0.855	21.77	0.659	0.122	63.38	45.07	0.5 / -0.6	
DMN_Maine_So	41	0.351	0.060	0.351	0.027	0.846	21.91	0.722	0.097	70.73	41.46	-1.7 / 6.2	
IER_Cinzana	117	0.349	0.049	0.383	0.016	0.878	24.01	0.757	0.060	58.97	36.75	0.9 / -0.9	
Djougou	29	0.501	0.057	0.712	0.031	0.905	29.17	0.618	0.061	27.59	13.79	-8.2 /-10.6	
Ilorin	35	0.507	0.040	0.774	0.030	0.867	32.30	0.468	0.145	28.57	8.57	-3.6 / 2.5	
Sede_Boker	184	0.225	0.049	0.152	0.012	0.815	67.64	0.793	0.105	25.54	9.78	-3.7 /-0.2	

[†]AERONET spectral AOD was interpolated to the MISR green-band wavelength for these comparisons (see text). The last column contains Version 12 results corresponding to the Biomass Burning, Continental, Dusty, and Maritime categories, though with a different selection sites and different sampling, from *Kahn et al.* [2005] (Paper 1). These data are from V22 of the aerosol product.

[§]This column contains two numbers. The first is the difference between the percent of MISR [Central + Surroundings] falling within 20% or 0.05 × AOD of the corresponding AERONET value, and the percent of MISR Central-only falling within this envelope. The second number is the same quantity, but calculated for the 10% or 0.03 × AOD envelope. For the categories overall (bold in this table), these quantities are plotted in Figure 2 along the vertical axis. (See text for details.)

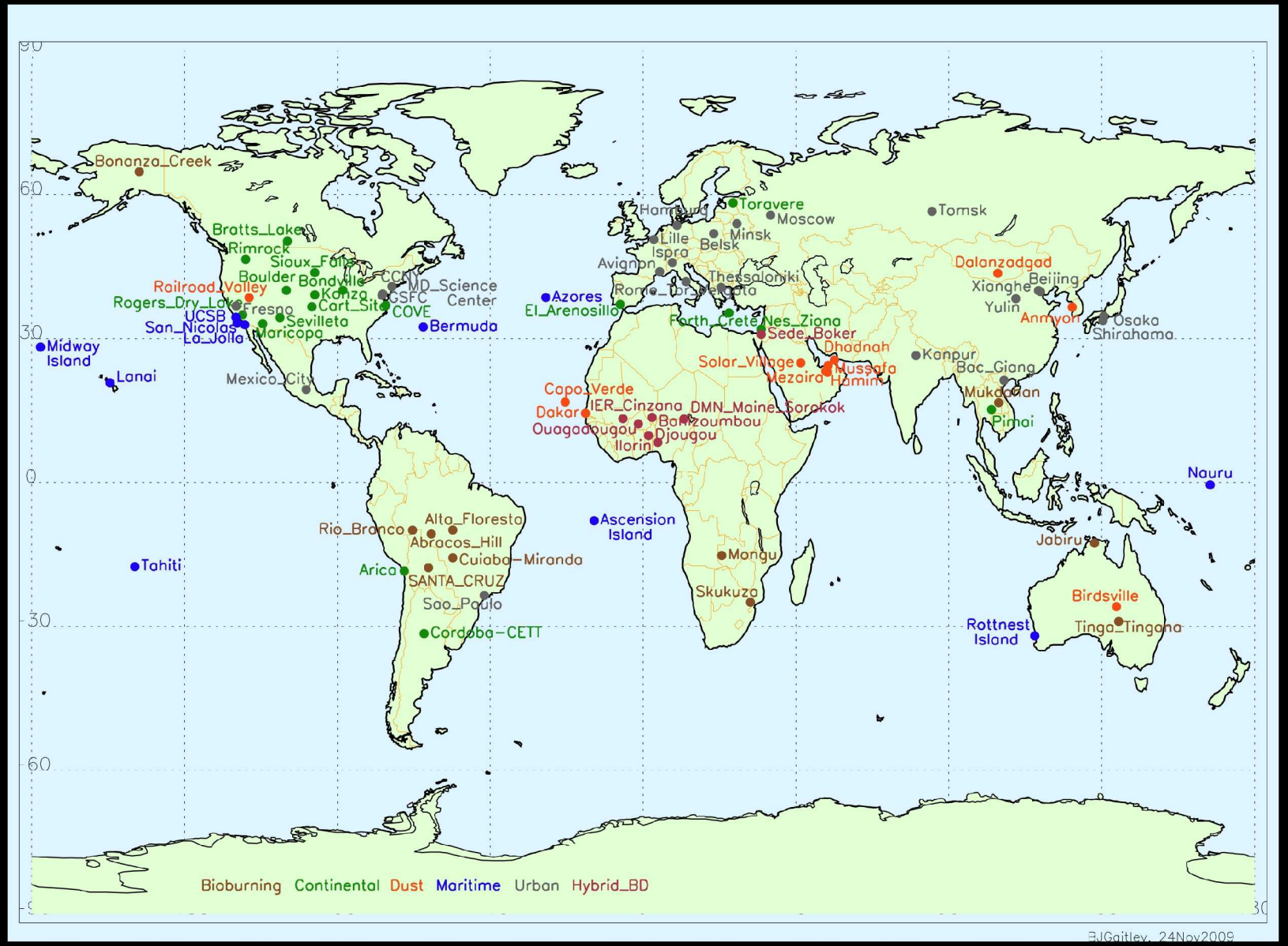
Bonanza_Creek
Bratts_Lake
Rimrock
Sioux_Falls
Boulder
Bondville
Railroad_Valley
Kanza
CCNY
MD_Science Center
GSFC
Rogers_Dry_Lake
Fresno
Cart_Site
COVE
UCSB
Sevilleta
San_Nicolas
Maricopa
La_Jolla
Bermuda
Midway Island
Lanai
Mexico_City
Tahiti
Rio_Branco
Alta_Floresta
Abracos_Hill
Cuiaba-Miranda
Arica
SANTA_CRUZ
Sao_Paulo
Cordoba-CETT
Ascension Island
Azores
El_Arenosillo
Harwell
Toravere
Moscow
Tomsk
Lille
Minsk
Belsk
Ispra
Avignon
Thessaloniki
Forth
Crete_Nes_Ziona
Sede_Boker
Dhadnah
Solar_Village
Mezaira
Hamim
Kanpur
Bac_Giang
Mukdahan
Pimai
Capo_Verde
Dakar
IER_Cinzana
DMN_Maine_Soroko
Banizoumbou
Ouagadougou
Djougou
Ilorin
Mongu
Skukuza
Dalanzadgad
Xianghe
Beijing
Yulin
Anmyon
Osaka
Shirahama
Nauru
Jabiru
Birdsville
Tinga_Tingana
Rottnest Island
Bioburning
Continental
Dust
Maritime
Urban
Hybrid_BD
BJGaitley, 24Nov2009

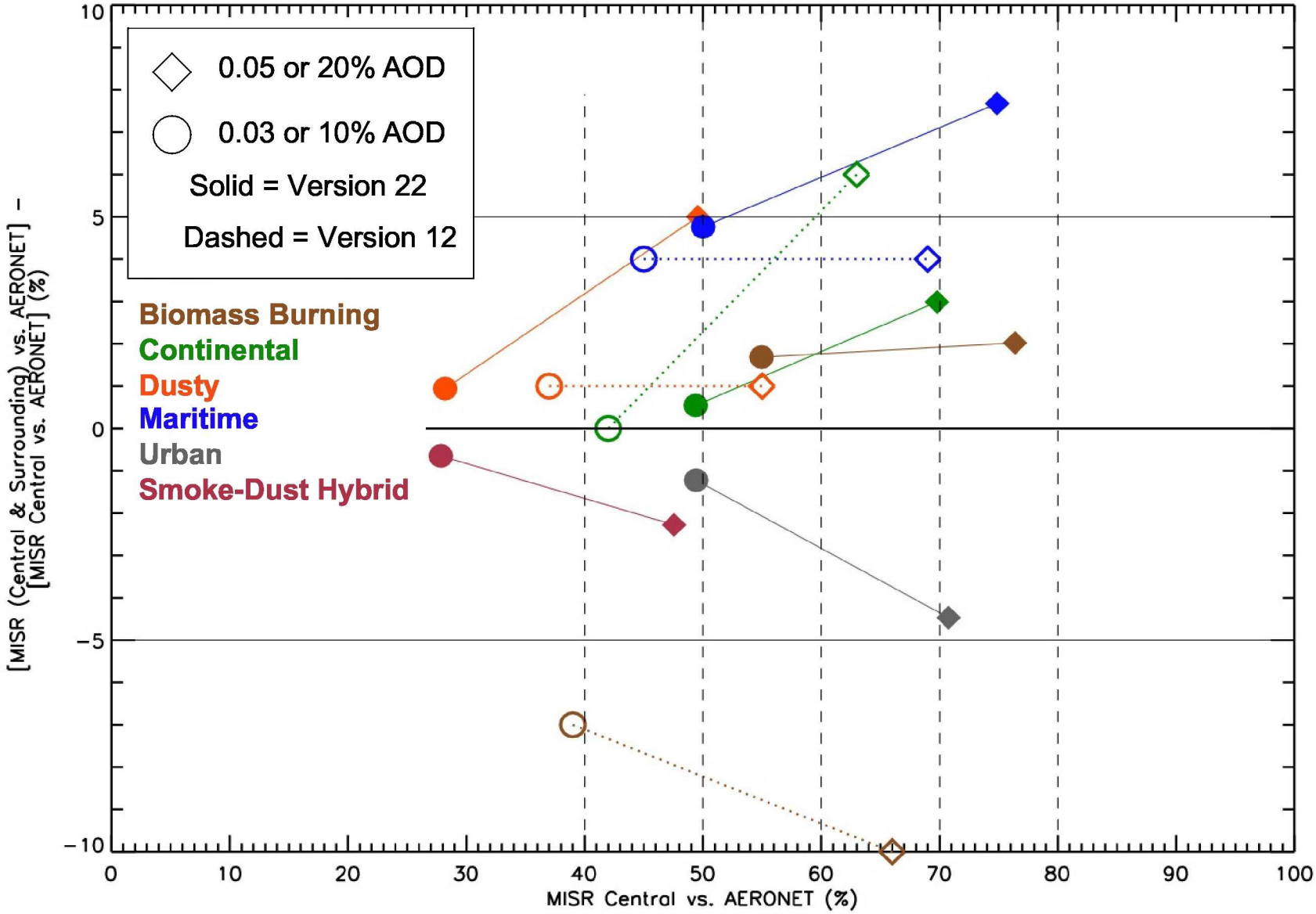
0.05 or 20% AOD
0.03 or 10% AOD
Solid = Version 22
Dashed = Version 12
Biomass Burning
Continental
Dusty
Maritime
Urban
Smoke-Dust Hybrid
[MISR (Central & Surrounding) vs. AERONET] – [MISR Central vs. AERONET] (%)
MISR Central vs. AERONET (%)
10
5
0
−5
−10
0
10
20
30
40
50
60
70
80
90
100

Figure 2

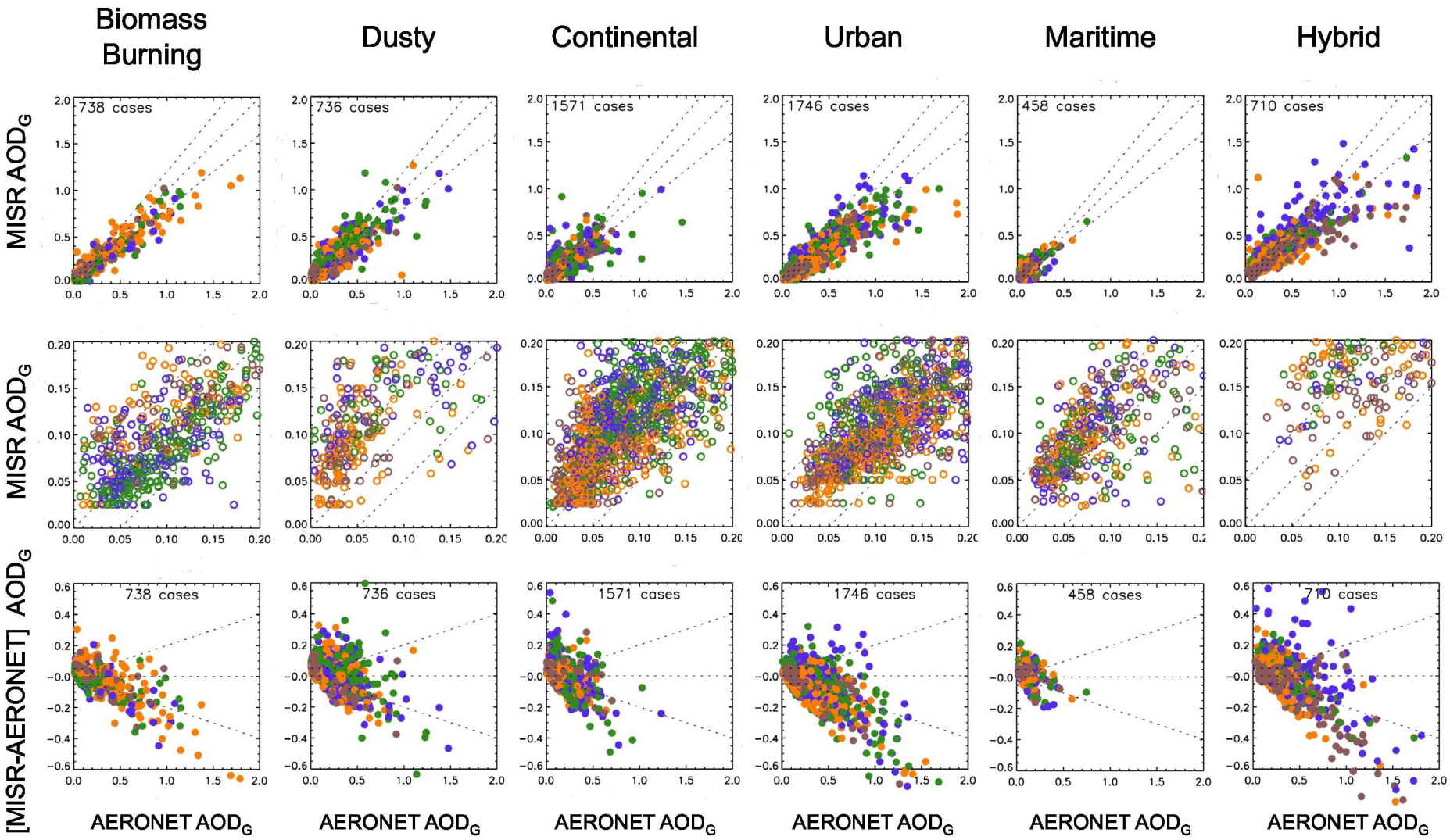
Biomass Burning
Dusty
Continental
Urban
Maritime
Hybrid
MISR AOD$_G$
MISR AOD$_G$
[MISR-AERONET] AOD$_G$
738 cases
736 cases
1571 cases
1746 cases
458 cases
710 cases
AERONET AOD$_G$
AERONET AOD$_G$
AERONET AOD$_G$
AERONET AOD$_G$
AERONET AOD$_G$
AERONET AOD$_G$

Figure 3

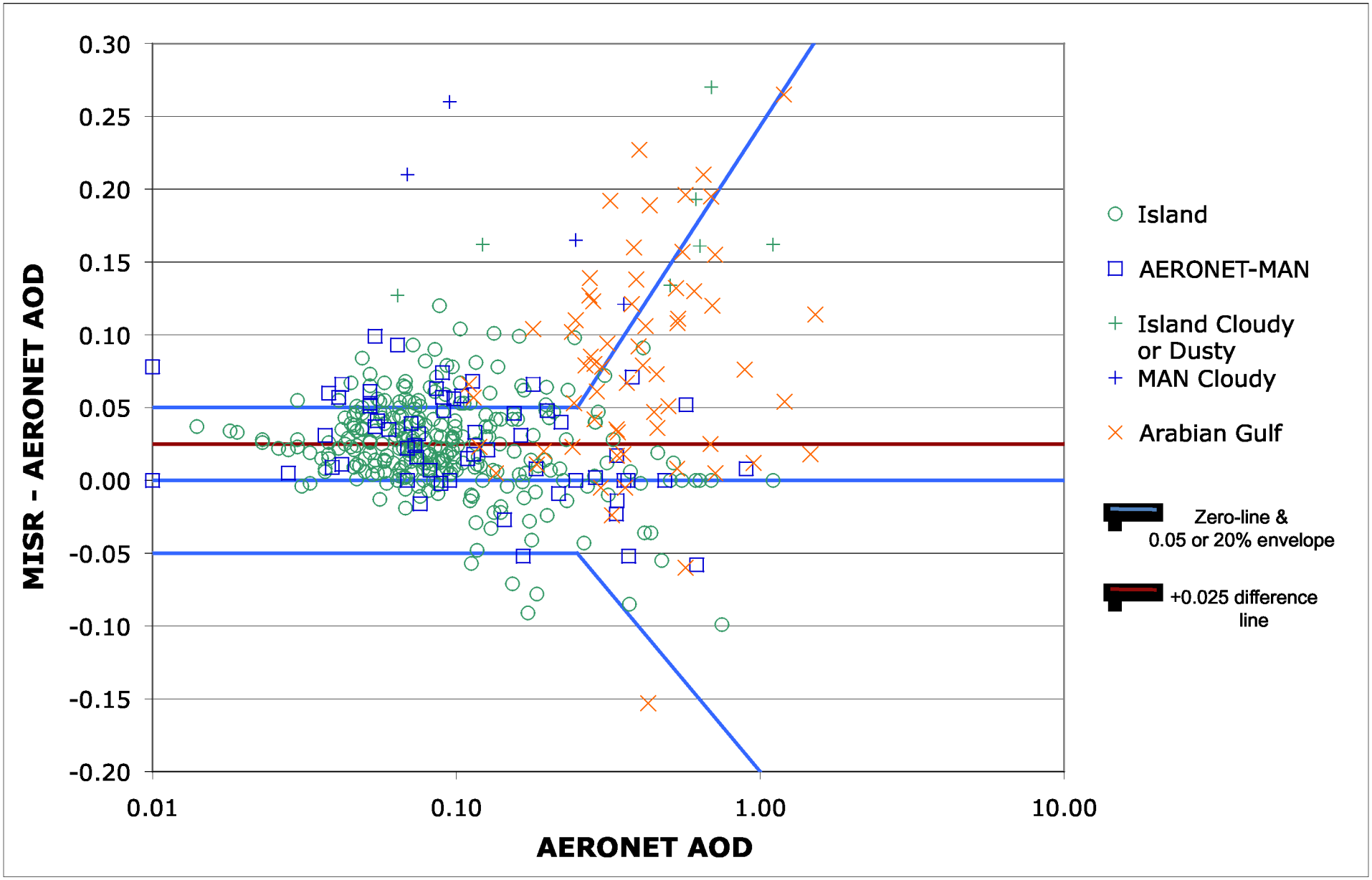
0.30
0.25
0.20
0.15
0.10
0.05
0.00
-0.05
-0.10
-0.15
-0.20
MISR - AERONET AOD
0.01
0.10
1.00
10.00
AERONET AOD
Island
AERONET-MAN
Island Cloudy or Dusty
MAN Cloudy
Arabian Gulf
Zero-line & 0.05 or 20% envelope
+0.025 difference line

Figure 4

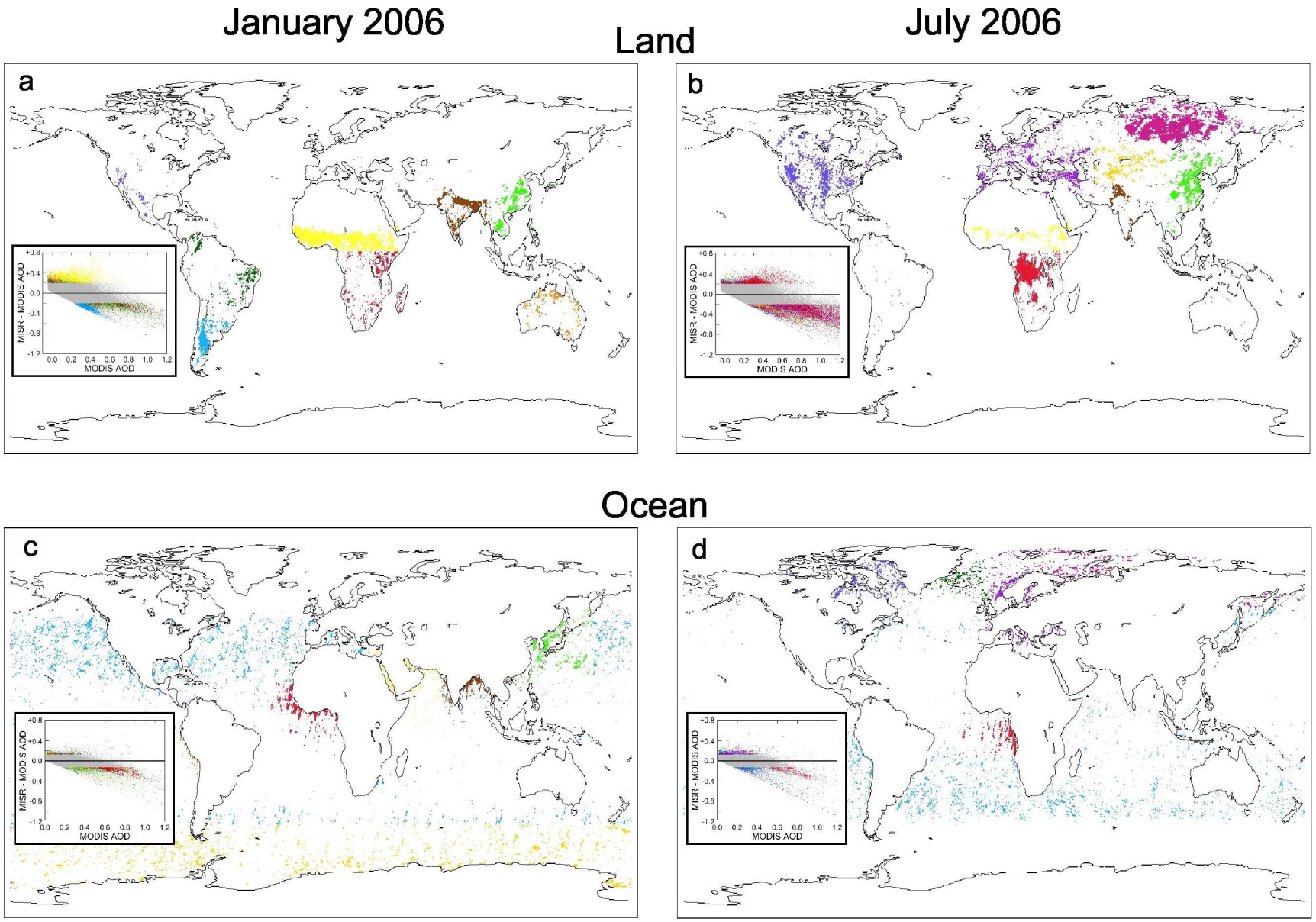
January 2006
July 2006
Land
Ocean
a
b
c
d
MISR - MODIS AOD
MODIS AOD
+0.8
+0.4
0.0
-0.4
-0.8
-1.2
0.0
0.2
0.4
0.6
0.8
1.0
1.2

Figure 5

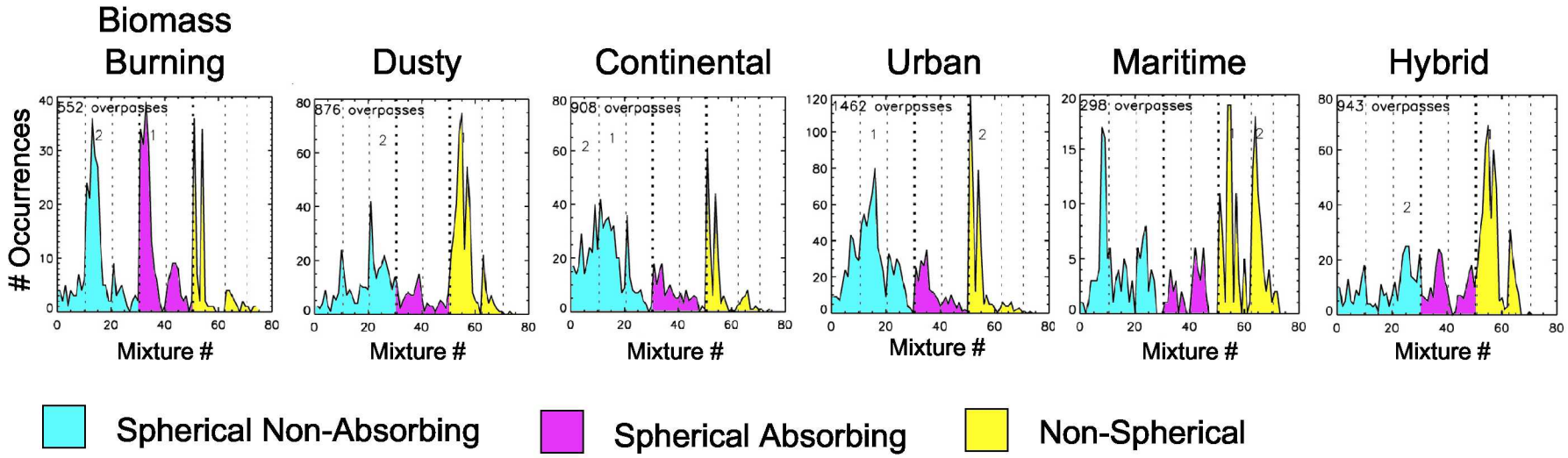
Biomass Burning
Dusty
Continental
Urban
Maritime
Hybrid
Occurrences
552 overpasses
876 overpasses
908 overpasses
1462 overpasses
298 overpasses
943 overpasses
Mixture #
Spherical Non-Absorbing
Spherical Absorbing
Non-Spherical

Figure 6

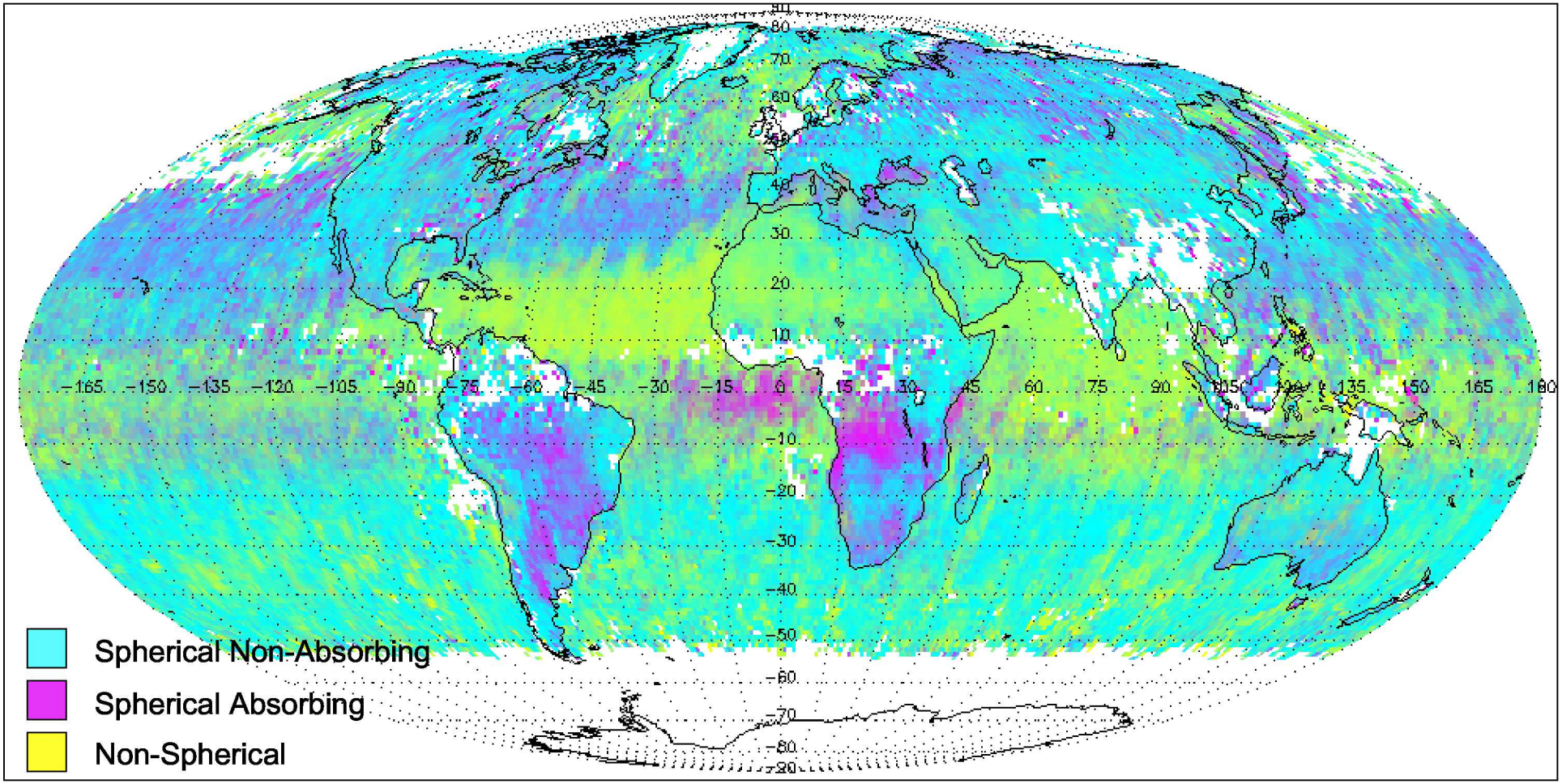
Spherical Non-Absorbing
Spherical Absorbing
Non-Spherical

Figure 7

738 Events at **Biomass Burning** Locations

736 Events at **Dusty** Locations

1571 Events at **Continental** Locations

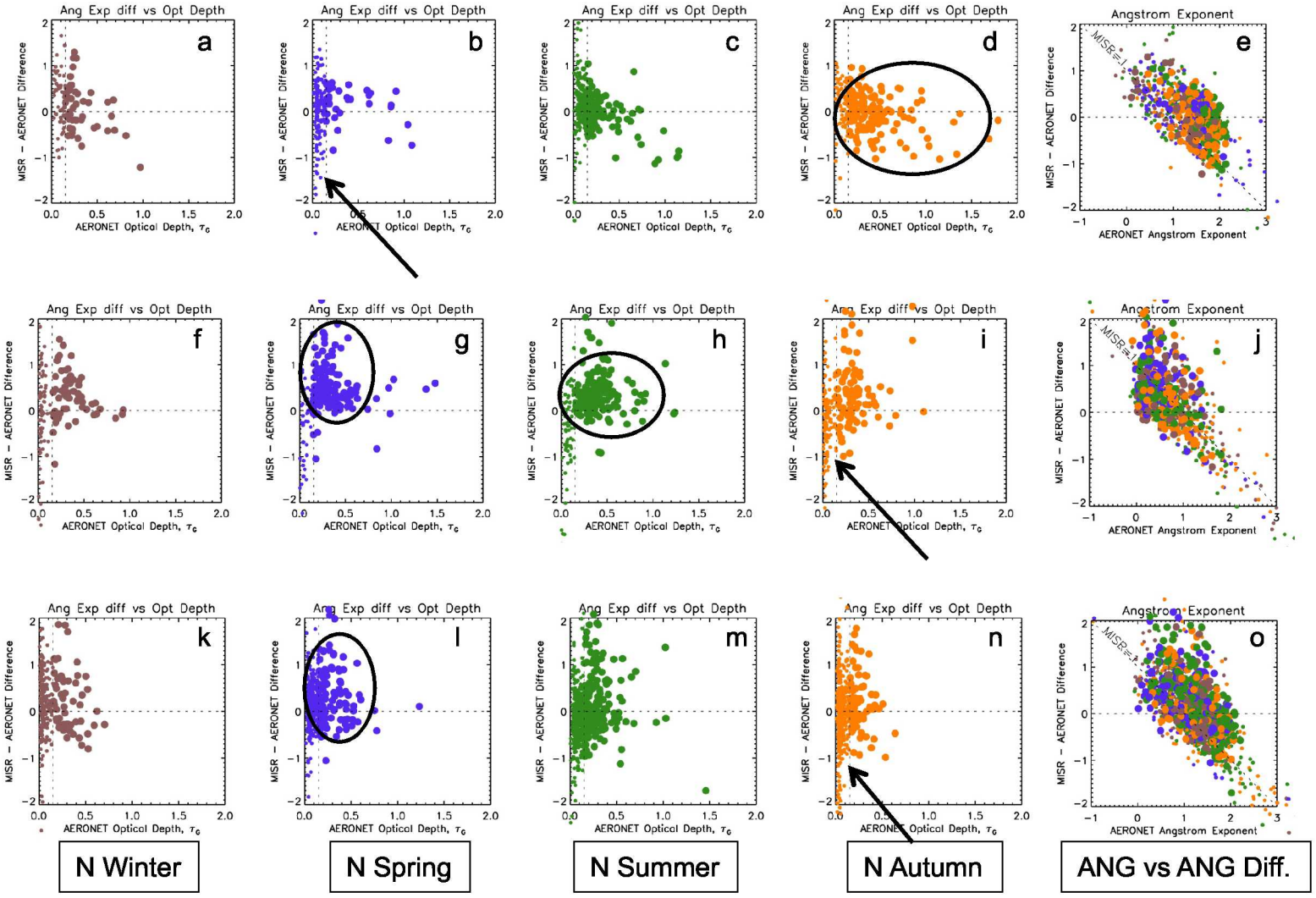

Figure 8

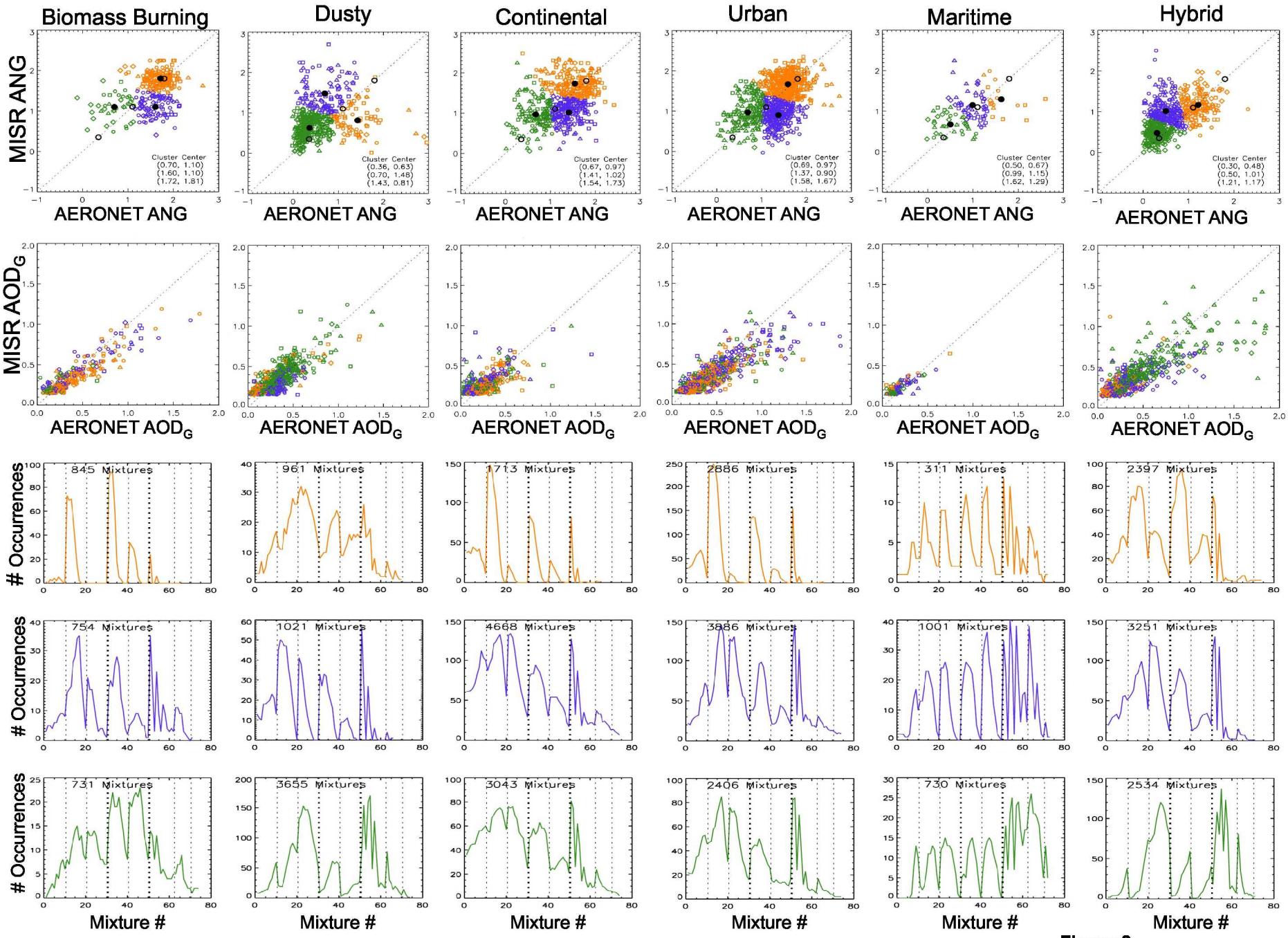
Biomass Burning
Dusty
Continental
Urban
Maritime
Hybrid
MISR ANG
AERONET ANG
Cluster Center (0.70, 1.10) (1.60, 1.10) (1.72, 1.81)
Cluster Center (0.36, 0.63) (0.70, 1.48) (1.43, 0.81)
Cluster Center (0.67, 0.97) (1.41, 1.02) (1.54, 1.73)
Cluster Center (0.69, 0.97) (1.37, 0.90) (1.58, 1.67)
Cluster Center (0.50, 0.67) (0.99, 1.15) (1.62, 1.29)
Cluster Center (0.30, 0.48) (0.50, 1.01) (1.21, 1.17)
MISR AOD$_G$
AERONET AOD$_G$
Occurrences
845 Mixtures
961 Mixtures
1713 Mixtures
2886 Mixtures
311 Mixtures
2397 Mixtures
754 Mixtures
1021 Mixtures
4668 Mixtures
3886 Mixtures
1001 Mixtures
3251 Mixtures
731 Mixtures
3655 Mixtures
3043 Mixtures
2406 Mixtures
730 Mixtures
2534 Mixtures
Mixture #

Figure 9